Chapter One

Introduction and Literature Review

1. 1 Introduction:

Modification of surface properties over multiple length scales plays an important role in optimizing a material's performance for a given application. For instance, the cosmetic appearance of a surface and its absorption properties can be controlled by altering its texture and presence of chemical impurities in the surface. Material's susceptibility to wear and surface damage can be reduced by altering its surface chemistry, morphology, and crystal structure. Also, one can consider the frictional, adhesive, and wetting forces acting at a material interface as being strongly influenced by the size and shape of the micro and nano-scale features present. As such, multi-scale surface modifications are a critical factor in the development of new material structures and in engineering the detailed interactions that occur at surfaces and interfaces. From the earliest work with pulsed ruby lasers, it has been understood that the unique interaction of laser light with a material can lead to permanent changes in the material's properties not easily achievable through other means. "Laser irradiation has been shown to induce changes to the local chemistry, the local crystal structure, and the local morphology, all of which affect how the material behaves in a given application" (Marouf et al., 2014, p.93).

Low-cost disposable optical components are of high demand for bio-medical and *in-vivo* applications. Integrated structures require reliable and often advanced inscription methods to create features such as waveguides and gratings in optical materials to form components of optical communication systems, sensor and optoelectronic devices. Femtosecond (fs) laser pulses are utilized to fabricate highly localized 3-D structures within transparent media, facilitating large penetration depths and forming submicron feature sizes due to non-linearity at ultra-high intensities. "Refractive index structures for photonic devices produced by direct writing with fs pulses are established in glass but are relatively unexplored in polymer materials, such as polymethyl methacrylate (PMMA)" (Alexandra et al.,2007, p.1).

Raman spectral imaging (or mapping) is a method for generating detailed chemical images based on a sample's Raman spectrum. A complete spectrum is acquired at each and every pixel of the image, and then interrogated to

generate false color images based on material composition and structure. Raman peak intensity yields images of material concentration and distribution, Raman peak position yields images of molecular structure and phase, and material stress/strain and Raman peak width yields images of crystallinity and phase.

A typical experiment uses sequential sample movement and spectrum acquisition, repeated hundreds, thousands or even millions of times, to collect data from the user defined image area.

Raman spectral images can be collected in two and three dimensions, to yield XY images, XZ and YZ slices, and XYZ data-cubes.

Raman spectral imaging is an invaluable technique for scientists in many varied fields, since it allows chemical distribution to be viewed which is invisible by standard optical microscopy.

The fast mapping Raman instrument is ideal for the study of any material having spatially varying chemical composition. Typical applications include:

Pharmaceutical products, Filled or composite materials, Analysis of defects and contamination, Material Morphology and Medical Devices

Raman spectroscopy is a non destructive optical technique which demonstrated here to measure laser induced photo chemical changes in the monomer content of surface photonic structures such as gratings and waveguides in bulk polymethyl methacrylate (PMMA).

PMMA based polymer optical fibre (POF) and optical components are inert, inexpensive, rugged, and thus ideal for disposable sensor devices in clinical, biological and chemical applications. In-fibre gratings formed in POF have advantages as sensors because the bulk thermo-optic, electro-optic and strain sensitivities of polymers are up to 10 times those of glass. The photomodification and ablation of PMMA based on linear absorption of UV continuous wave and excimer laser are well studied processes , however, their low penetration depth limits 3D applications. Ultra-short pulsed laser refractive index modification of PMMA to date employs the nonlinear absorption of the fundamental Ti:Sapphire laser wavelength around 800 nm. Whereas other refractive index structuring methods often require photosensitization, Scully *et al*. showed that commercial grade PMMA can be readily photomodified by fs irradiation , a clean procedure requiring neither pre-nor post-processing. Low dose excimer laser experiments showed that

nanosecond photochemical processes in PMMA produce positive as well as negative refractive index changes . “Initial wave guide structures in PMMA using 800 nm, fs laser pulses reported differing results about the sign of the refractive index change” (Taranu et al., 2010, p.1).

Silicon is the most commonly used semiconductor in optoelectronic devices and Silicon photodiodes are extensively used in industrial applications as reliable devices for light to electricity conversion. These features are especially important in the field of optical radiometry in which measurements of photometric and radiometric quantities have to be done with a high level accuracy. The crystalline silicon is the most important material in the photovoltaics today. According to predictions it will remain an important and dominant material in photovoltaics over the next 10-30 years, owing to its well recognized properties and its established production technology .

The laser direct-write technique is an established method for the fabrication of photonic waveguide systems in dielectric media such as single and multi component glasses. Examples of devices fabricated include 3-dimensional waveguide networks, couplers, Bragg gratings, optical amplifiers and lasers. This technique will be used here to form photo-chemical and optical density changes in polymethyl methacrylate.

Surface spatial mapping of the photo-thermal changes in the structures formed by direct laser writing on PMMA by means of a CW diode laser with 0.3 Watt power at 810 nm wavelength of operation was demonstrated. Silicon irradiated at 1 kHz repetition rate, for 180fs at 387nm and 44 fs at 800nm doesn't need Raman mapping. Two Raman transitions can be observed in Raman spectra of irradiated with fs lasers PMMA samples. A transition located at 1640 cm^{-1} indicates a stretching mode of the C=C bond present only in the monomer and the transition located at 1725cm^{-1} indicates a stretching mode of C=O bond present in monomer and polymer. The ratio of their Raman peak intensities gives a measure of monomer content present inside the sample. “Decreases in this monomer content after laser irradiation, are related to main chain scission and unzipping, molecular weight decrease and decreased refractive index. Increases in monomer proportion indicate cross-linking and the refractive index increased” (Taranu et al., 2010, p.1).

1.2. Literature review:

Zoubir *et al* (2002) showed the ability of femtosecond material micro-processing to produce very fine surface structures and its versatility both in the type of processing and the type of materials to be processed. Comparison between the femtosecond and nanosecond regimes has shown one more time that finer, more energy-effective and more material-independent structuring could be obtained with femtosecond pulses.

Zoubir *et al* (2003) described the ablation dynamics in two types of silicate glasses having different compositions. The differences observed were explained by the self-focusing effect. Examples of device fabrication illustrate the practical use of femtosecond material processing.

Florea *et al* (2003) reported both straight and curved waveguides written in a variety of silicate glasses using near-IR femtosecond laser pulses. Writing parameters are identified that produce waveguides that support only a single mode and yield smooth-mode profiles. The laser pulse-induced refractive index change is reconstructed from near-field mode profile data using the scalar wave equation and by refractive near-field profiling. Both coarse and fine period gratings are written and characterized, and the thermal stability of these gratings is investigated. The utility of the femtosecond writing technique is demonstrated by fabricating an optical interleaver.

Cheng (2004) reported sporadically the surface chemistry modification of PMMA using direct-write laser micromachining to fabricate microfluidic chips. The method developed does not require extensive solvent drying procedures and is therefore simpler and more efficient than existing methods. Organosilane modification largely expands the application of the PMMA as a biochip substrate for that a great variety of surface functional groups can be prepared on the plastic surface with similar procedure. Perfluoroalkylation modification can be used for surface passivation of PMMA to prevent adsorption. Aminoalkylationand mercaptoalkylation have been used for biomolecule immobilization.

Zoubir *et al* (2004) fabricated buried tubular waveguides having an annular core in bulk PMMA by femtosecond laser direct writing. The refractive index profile was obtained from selective etch profiling. Numerical calculation of the propagating modes in the waveguides was performed with a finite-difference method. Good agreement was found between calculation and measurement of the output distribution in the near field.

Kro *et al* (2004) reviewed their work on fs-laser fabrication and characterization of photonic structures in glass and discuss the effect of glass composition on processing parameters and structural modification.

Tan *et al* (2005) presented a direct ablation technique for the fabrication of gratings by interfering femtosecond pulses in a specially designed optical configuration. This technique ensures that gratings are formed only at the focal point. The grating line-width can be varied with minor adjustment to the optical configuration. This configuration not only simplifies the optical set-up, but also immunizes the system to extraneous and inherent vibrations, thus enabling gratings of good edge acuity. With this technique, they have successfully fabricated planar gratings of different line-widths on a silicon substrate. This method offers a new approach of the fabrication of a grating on a surface by direct ablation. Also, the feasibility of effectively writing internal gratings in transparent materials is discussed.

Kazuyoshi (2006) studied the refractive index changes and vacancies that are induced in transparent materials like glass by the irradiation of femtosecond laser pulses. He applied this technique to fabricate three-dimensional photonic structures such as optical data storages, waveguides, gratings, and couplers inside a wide variety of transparent materials. He reported micro-fabrication experiments of optical elements in glasses with femtosecond laser pulses, including fabrication of couplers, Bragg gratings, and zone plates and holograms on the surface of glass. A trial fabrication experiment on organic materials is also reported.

Krishnan *et al* (2006) reported the development of high quality dense alumina coatings for providing electrical insulation for DC induction pumps of PFBR. Utility of high power lasers to transform the metastable γ-Al_2O_3 phase present in as-deposited Air Plasma Sprayed (APS) alumina coatings into thermodynamically stable α-Al_2O_3 phase is demonstrated. A host of solid-state analytical techniques including non-destructive laser based optical techniques that have the potential for on-line adaptation have been developed in-house.

Marshall *et al* (2006) include optical waveguides that incorporate Bragg gratings written in bulk fused silica by using the femtosecond laser direct-write method and without the need for lithography or ion-beam techniques. A single manufacturing process is used to create waveguide–Bragg grating reflectors for operation in the C band.

Arnold & Piqué (2007) illustrated the range of materials processing capabilities, fundamental research opportunities, and commercially viable applications that can be achieved using recently developed laser direct-write techniques.

Dongre *et al* (2007) characterized optical waveguides fabricated by irradiation of a glass substrate with femtosecond laser pulses and their potential application to integrate on-chip optical detection with glass-based lab-on-chip systems. A number of properties critical for the application of these waveguides in optical sensing were characterized. The results indicate that such integration is indeed feasible. The thorough understanding of the waveguide properties provides an important input for the design of integrated sensing devices on a commercial lab-on-chip system for exploitation of these two glass-based technologies.

Dobrzański & Drygała (2008) found that the method of texturing of multicrystalline silicon surface using Nd:YAG laser appeared to be much more independent on grains crystallographic orientation compared to conventional texturing methods. Laser texturing makes it possible to increase absorption of the incident solar radiation.

Vishnubhatla *et al* (2008) fabricated micro gratings in silicate, Foturan ™, and tellurite glasses using femtosecond direct writing. Refractive index change in these structures was estimated using optical diffraction technique and was found to be in the order of 10^{-3} sufficient for wave guiding applications. The ability to create such structures, both passive and active, has strong implications in the field of micro-photonic and microfluidic devices.

Taranu *et al* (2010), demonstrated the Spatial mapping of photo-chemical and optical density changes in polymethyl methacrylate formed by direct femtosecond laser writing of photonic structures at 180 fs, 387nm and 44fs, 800 nm at 1kHz repetition rate. Their Results show the variations in the monomer content and intensity of background scattering light in the substructure. They noted that this technique needs further refinement but these initial results indicate that it is useful for polymer optical fibres (POF) because it enables the photo-chemical and optical density composition of subsurface photonic structures to be estimated non invasively and refractive index to be estimated.

Taleb *et al* (2011), investigated and demonstrated the experimental evidence of the effect of femtosecond laser pulses on the spectral response of a Silicon photovoltaic cell. The observed enhancement is related

to the appearing of nano-structured groves in the 700-900 nm range. The responsivity and the conversion efficiency of the photovoltaic cell are enhanced by this technique. Ultrashort laser pulses should be still economically reasonable in a large scale production.

Deepak *et al* (2011) investigated femtosecond laser induced microstructures, gratings, and craters in four different polymers: poly methyl methacrylate (PMMA), poly dimethyl siloxane (PDMS), polystyrene (PS) and poly vinylalcohol (PVA). They studied local chemical modifications leading to the formation of optical centers and peroxide radicals, and demonstrated some of the possible applications of laser direct writing towards waveguides, Y couplers, and memory based devices.

Bauma *et al* (2011) reportd on the fabrication of optical Bragg type phase gratings in polymethyl methacrylate substrates by a femptosecond Ti: Sapphire laser. As for their optical characterization, a spatially resolved microscopy interferometric technique is used to investigate the two-dimensional distribution of the refractive index change produced by the irradiation process. The results suggest that efficient modification of the material can be accomplished for a regime of repeated pulses with long pulses, 250 fs with low laser fluency.

Fernandes *et al* (2011) harnessed femtosecond laser induced birefringence in fused silica waveguides for the first time to demonstrate polarization beam splitting in buried optical circuits. Moderately strong extinction ratio of up to -24 dB was noted for 2 cm long devices. The polarization beam splitters are sufficiently wavelength selective to be attractive for wavelength-division multiplexing (WDM) application and promise to open new directions for creating polarization dependent devices in three dimensional optical circuits, and reported that the means to extend the bandwidth for such polarization splitting will require further design and laser process development.

Oliveira *et al* (2012) reported on a simple method to obtain surface gratings using a Michelson interferometer and femtosecond laser radiation. In the optical setup used, two parallel laser beams are generated using a beam splitter and then focused using the same focusing lens. An interference pattern is created in the focal plane of the focusing lens, which can be used to pattern the surface of materials. The main advantage of this method is that the optical paths difference of the interfering beams is independent of the distance

between the beams. The potential of the method was demonstrated by patterning surface gratings with different periods on titanium surfaces in air.

Teixidor *et al* (2012) reported an investigation on the effects of nanosecond laser processing parameters on the depth and width of microchannels fabricated from poly methylmethacrylate (PMMA). The Nd:YAG solid-state pulsed laser has a wavelength of 1064 nm and a measured maximum power of 4.15 W. The laser processing parameters are varied. Main effects plots and microchannel images are utilized to identify the effects of the process parameters for improving material removal rate and surface quality simultaneously for laser micromachining of microchannels in PMMA polymer. It is observed that channel width and depth decreased linearly with increasing Q-switch delay time (hence average power) and increased nonlinearly with increasing scanning rate and not much affected by the increase in pulse frequency.

Horn *et al* (2012) reported the fabrication of femtosecond laser-induced, first-order waveguide Bragg gratings in lithium niobate in the low repetition rate regime. Type-II waveguides are written into an x-cut lithium niobate wafer and structured periodically to achieve narrowband reflections at wavelengths around 1550 nm. Additionally, electrodes are employed to allow for electro-optic tuning of the spectral response. And demonstrate wavelength control of the central reflection peak by applying a static external electric field. A maximum shift of the reflection peak of $\Delta\lambda$=625 pm is observed.

Buividas *et al* (2012) reported in high-precision surface ablation, film removal, ripple formation are presented. They discussed volume processing via polymerization, marking, dicing, cutting, and drilling of semiconductor and dielectric materials. And focused on processes which can be carried out at a high throughput in the industrial environment or/and can deliver functionalities currently not amenable by competing technologies. Unique features of direct laser writing by femtosecond laser pulses are highlighted. Methodology for solutions of engineering tasks is presented. Namely, the laser irradiation parameters are selected on the basis of the required processing conditions for the material of a work-piece.

Deepak *et al* (2012) investigated femtosecond-laser-induced microstructures (on the surface and within the bulk), gratings, and craters in four different polymers: polymethyl methacrylate, polydimethylsiloxane, polystyrene, and polyvinyl alcohol. Local chemical modifications leading to

the formation of optical centers and peroxide radicals were studied using ultraviolet-visible absorption and emission, confocal micro-Raman and electron spin resonance spectroscopic techniques. Potential applications of these structures in microfluidics, waveguides, and memory-based devices are demonstrated.

Deepak *et al* (2012) investigated formation of defects in four polymers namely Poly (methylmethacrylate) [PMMA], Poly dimethylsiloxane [PDMS], Polystyrene [PS], and Polyvinyl alcohol [PVA] and crystal media such as Lithium Niobate [$LiNbO_3$]. Pristine polymers are not paramagnetic, but exhibited paramagnetic behavior upon fs irradiation. $LiNbO_3$ (LNB) crystal has not shown any defect formation upon laser irradiation.

Deepak *et al* (2013) reported spectroscopic properties of fs laser irradiated polymers and LNB crystal. In case of polymers observed emission from the fs laser modified regions and it is found to be shifting with the excitation wavelength due to various transitions involved in functional groups and red edge effect. Also these materials exhibited paramagnetism upon fs laser irradiation unlike LNB crystal. Confocal micro Raman studies revealed broadening in case of polymers which is an indication of the presence of radicals and or defects which are confirmed through emission and ESR studies. Fs laser irradiated LNB crystal also showed the presence of defects but they do not exhibit the properties of emission and paramagnetism (like polymer media) due to absence of functional groups.

Marouf *et al* (2014) utilized a fast laser texturing technique to produce micro/nano surface textures in Silicon by means of UV femtosecond laser pulses. They demonstrated and investigated the experimental evidence of the effect of femtosecond laser pulses on the spectral response of a Silicon photovoltaic cell, and found that the use of this method leads to improve the responsivity and the conversion efficiency of the photovoltaic cell. The irradiation process leads to the formation of Micro- Nano meter periodic structure on substrates with a large area using single or double exposition. This technique is much cheaper and simpler than the electron beam lithography.

1.3. Objectives:

This work aimed mainly to:

- Obtain a textured surface in Polymethylmethacrylate (PMMA) by means of IR diode laser, 0.3 Watt power at 810 nm wavelength, and a textured

surface on Silicon photovoltaic cell (Si) at 1kHz repetition rate, for two laser wavelengths: 180fs at 387nm and 44 fs at 800nm.

- Fabricating surface gratings from PMMA by employing a homemade laser direct writing machine.
- Characterization of the induced surface texturing by means of Raman spectrometer.
- Demonstrating the effect of texturing on the spectral response of the silicon photovoltaic cell.

1.4. Thesis formatting:

The thesis comprises of four chapters; chapter one contains a short introduction to surface modification and previous studies. Chapter two involves a detailed theoretical background and basic concepts of Laser Direct Writing (LDW) Processing, Laser Material Interaction and Raman Spectroscopy. The experimental part is fully described and presented in chapter three. Then the results had been presented, analyzed and discussed in chapter four and finally a short conclusion of this research and recommendations were presented and followed by a list of References.

Chapter Two

Theoretical Background

2.1 Poly(methyl methacrylate) (PMMA):

Polymethylmethacrylate (PMMA), a clear plastic, is a pretty versatile material. Plexiglas windows are made from PMMA. Acrylic paints contain PMMA. It also remains one of the most enduring materials in orthopedic surgery where it has a central role in the success of total joint replacement. Being part of a group of medical materials called 'bone cement', its use includes the fixation of biomaterials such as artificial joints to bone, the filling of bone defects and, also, as a drug-delivery system (Manoj et al., 2012).

Poly(methacrylates) are polymers of the esters of methacrylic acids. The most commonly used among them is poly (methyl methacrylate) (PMMA). Poly (methyl methacrylate) or poly (methyl 2-methylpropenoate) is the polymer of methyl methacrylate, with chemical formula $(C_5H_8O_2)_n$. It is a clear, colorless polymer available on the market in both pellet and sheet form under the names Plexiglas, Acrylite, Perspex, Plazcryl, Acrylplast, Altuglas, Lucite etc. It is commonly called acrylic glass or simply acrylic. Another polymer, poly(methyl acrylate) (PMA) is a rubbery material, similar to poly(methyl methacrylate), but softer than it, because its long polymer chains are thinner and smoother and can more easily slide past each other.

2.1.1 Structure

Poly(methyl methacrylate) is produced by free-radical polymerization of methylmethacrylate in mass (when it is in sheet form) or suspension polymerization according to the following chart:

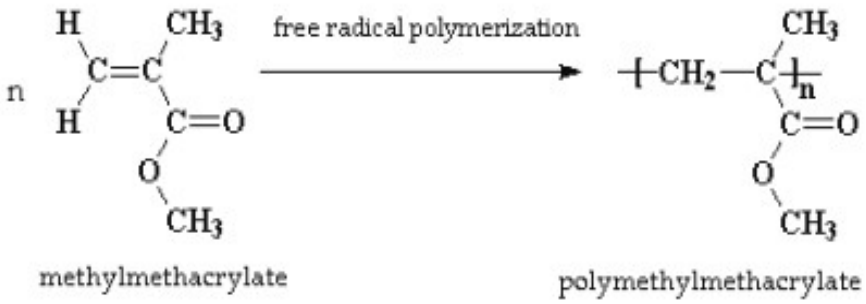

Figure 2.1: A chart of free-radical polymerization of methylmethacrylate

2.1.2 Physical and mechanical properties of PMMA:

PMMA is a linear thermoplastic polymer. PMMA has a lack of methyl groups on the backbone carbon chain - its long polymer chains are thinner and smoother and can slide past each other more easily, so the material becomes softer. Main physical characteristics of PMMA are shown in table 2.1.

Table 2.1 Typical physical properties of Polymethyl methacrylate.

Physical Properties	Value
Density	1.15 - 1.19 g/cm3
Water Absorption	0.3 – 2 %
Moisture Absorption at Equilibrium	0.3 - 0.33 %
Linear Mould Shrinkage	0.003 - 0.0065 cm/cm
Melt Flow	0.9 – 27 g/10 min

PMMA has high mechanical strength, high Young's modulus and low elongation at break. It does not shatter on rupture. It is one of the hardest thermoplastics and is also highly scratch resistant. It exhibits low moisture and water absorbing capacity, due to which products made have good dimensional stability. Both of these characteristics increase as the temperature rises. Table 2.2 shows some of mechanical characteristics of PMMA.

Table 2.2 Mechanical characteristics of Polymethyl methacrylate

Mechanical Properties	Value
Hardness, Rockwell M	63 - 97
Tensile Strength, Ultimate	47 - 79 MPa
Elongation at Break	1 - 30 %
Tensile Modulus	2.2 - 3.8 GPa
Flexural Modulus	3 - 3.5 GPa
Izod Impact, Notched	1.2 – 20k J/m
Izod Impact, Unnotched	11kJ/m
Tensile Creep Modulus, 1 h	1800 - 2700 MPa
Tensile Creep Modulus, 1000	h 1200 - 1800 MPa

Its strength properties during injection moulding differ significantly in longitudinal and transverse direction as a result of the orientation effect. As in the case with other thermoplastics, the mechanical properties of PMMA vary as the temperature changes. This material tends to creep. It is not suitable for operation under multiple dynamic loads.

PMMA is one of the polymers that is most resistant to direct sunshine exposure. Its strength characteristics exhibit fairly small variations under the effect of UV-radiation, as well as in the presence of ozone. These properties of PMMA make it suitable for products intended for long open-air operation.

2.1.3 Electrical characteristics of PMMA:

The low water absorption capacity of PMMA makes it very suitable for electrical engineering purposes. Its dielectric properties are very good, but polystyrene and LDPE are superior to it. Its resistivity depends on the ambient temperature and relative humidity. The dielectric constant, as well as the loss tangent, depends on the temperature, the relative humidity of air and the frequency. Table 2.3 shows some of Electrical characteristics of PMMA.

Table 2.3 Electrical properties of Polymethyl methacrylate.

Electrical Properties	Value
Electrical Resistivity	10^{14} - 10^{15} Ω.cm
Surface Resistance	10^{14} - 10^{16} Ω
Loss factor, 20°C, 1000 Hz, 60% humidity	0.04
Dielectric Constant	2.8 - 4
Dielectric Constant, Low Frequency	3 - 4
Dielectric Strength	17.7 - 60 kV/mm
Dissipation Factor	0.03 - 0.55
Arc Resistance	**2** - 180 s

2.1.4 Thermal properties of PMMA:

The thermal stability of standard PMMA is only 65ºC. Heat-stabilized types can withstand temperatures of up to 100ºC. PMMA can withstand temperatures as low as -70ºC. Its resistance to temperature changes is very good.

PMMA is a combustible material, which continues burning even after the flame is removed – the products separated in the process of thermal destruction have an intoxicating effect.

Table 2.4 Thermal properties of Poly (methyl methacrylate)

Thermal Properties	Value
CTE, linear 20°C	60 - 130 µm/m.°C
CTE, linear 20°C Transverse to Flow	70 - 90 µm/m.°C

Specific Heat Capacity	1.46 - 1.47 J/g.°C
Thermal Conductivity	0.19 - 0.24 W/m.K
Maximum Service Temperature, Air	41 - 103 °C
Melting Point	130°C
Vicat Softening Point	47 - 117 °C
Glass Temperature	**2** - 105 °C

2.1.5 Optical properties of PMMA:

PMMA exhibits very good optical properties – it transmits more light (up to 93% of visible light) than glass. Combined with its good degree of compatibility with human tissue, it can be used for replacement intraocular lenses or for contact lenses. Unlike glass, PMMA does not filter ultraviolet light. It transmits UV light down to 300 nm and allows infrared light of up to 2800 nm to pass.

Table 2.5 Optical properties of Polymethyl methacrylate.

Optical Properties	Value
Haze	1 - 96 %
Transmission, Visible	80 - 93 %
Refractive Index	2.1 - 1.498

2.1.6 Chemical resistance of PMMA:

Acrylics are unaffected by aqueous solutions of most laboratory chemicals, by detergents, cleaners, dilute inorganic acids, alkalis, and aliphatic hydrocarbons – however, acrylics are not recommended for use with chlorinated or aromatic hydrocarbons, esters, or ketones. It dissolves completely in chloroform, di- and trichlorethane, which is used for production of glues. The chemical resistance will vary with stress level, temperature, reagents and duration of exposure.

PMMA are physiologically harmless. Due to their low moisture absorption capacity they are not attacked by moulds and enzymes.

2.1.7 Processing methods of PMMA:

PMMA is suitable for injection moulding, extrusion, extrusion blow moulding (impact modified acrylics only), thermoforming, casting. The melt flow index of the material varies according to the method of treatment:

− Low melt flow index (0.8 – 2.5) – materials intended for extrusion;

− Medium melt flow index (2.5 - 10) – general-purpose PMMA;

− High melt flow index (> 10) – PMMA for injection moulding of products having a complex shape.

For injection moulding the mould temperature should be between 40 and 80ºC, depending on the type, the material temperature should be between 200 and 250ºC. Usually high injection pressures are needed because of poor flow properties. This is particularly important for optical mouldings where visible weld lines will form if the correct parameters are not used. During injection moulding internal stresses often build up, which can be eliminated by heating at a temperature about 80°C (tempering).

Mould's nozzle is an important factor when manufacturing PMMA-product. The size of the nozzle gate varies depending on the shape and the size of the product. Products manufactured from PMMA are mainly clear and transparent and it is important that they do not have any scratches. So that it is recommend to use at least draft angle of 1° (rather 2°). Because PMMA has high viscosity, the gas removing channels can be quite deep, from 0.04 to 0.08 mm.

Misoperation due to higher temperature causes destruction of PMMA, accompanied by release of methylmethacrylate or other low-molecule volatile products. The process also leads to a loss of mass, which makes it undesirable, and a good knowledge of the thermo-physical properties of the polymer is necessary in order to avoid it, especially in the temperature range processing (220-250°C).

Acrylics are easily sawed, drilled, milled, engraved, and finished with sharp carbide-tipped tools. Cut surfaces may be readily sanded and polished. They are also readily bent or thermoformed at low temperature and solvent bonding of properly fitting parts produces a strong, invisible joint. PMMA can be welded by all the plastics welding processes such as hot-blade, hot-gas, ultrasonic or spin welding.

2.1.8 Applications of PMMA:

PMMA is an economical, versatile general-purpose material. It is available in extruded and/or cast material in sheet, rod and tube forms, as well as custom profiles. Various types of acrylics are used in a wide variety of fields and applications, including:

- Optics: Dust covers for hi-fi equipment, sun-glasses, watch glasses, lenses, magnifying glasses;
- Vehicles: Rear lights, indicators, tachometer covers, warning triangles; Electrical engineering: Lamp covers, switch parts, dials, control buttons; Office equipment: Writing and drawing instruments, pens;
- Medicine: Packaging for tablets, pills, capsules, suppositories, urine containers, sterilisable equipment;
- Others: Leaflet dispensers, shatter-resistant glazing, shower cubicles, transparent pipelines, illuminated signs, toys (Harper & Charles, 2005).

2.2 Silicon (Si):

Silicon is a chemical element with the symbol Si and atomic number 14. It is a tetravalent metalloid, less reactive than its chemical analog carbon, the nonmetal directly above it in the periodic table, but more reactive than germanium, the metalloid directly below it in the table. Controversy about silicon's character dates to its discovery; it was first prepared and characterized in pure form in 1823. In 1808, it was given the name silicium (from Latin: *silex*, hard stone or flint), with an -ium word-ending to suggest a metal, a name which the element retains in several non-English languages. However, its final English name, first suggested in 1817, reflects the more physically similar elements carbon and boron.

Silicon is the eighth most common element in the universe by mass, but very rarely occurs as the pure free element in nature. It is most widely distributed in dusts, sands, planetoids, and planets as various forms of silicon dioxide (silica) or silicates. Over 90% of the Earth's crust is composed of silicate minerals, making silicon the second most abundant element in the Earth's crust (about 28% by mass) after oxygen.

Most silicon is used commercially without being separated, and indeed often with little processing of compounds from nature. These include direct industrial building-use of clays, silica sand and stone. Silica is used in ceramic brick. Silicate goes into Portland cement for mortar and stucco, and when combined with silica sand and gravel, to make concrete. Silicates are also in white-ware ceramics such as porcelain, and in traditional quartz-based soda-lime glass. More modern silicon compounds such as silicon carbide form abrasives and high-strength ceramics. Silicon is the basis of the ubiquitous synthetic silicon-based polymers called silicones.

Elemental silicon also has a large impact on the modern world economy. Although most free silicon is used in the steel refining, aluminium-casting, and fine chemical industries (often to make fumed silica), the relatively small portion of very highly purified silicon that is used in semiconductor electronics (< 10%) is perhaps even more critical. Because of wide use of silicon in integrated circuits, the basis of most computers, a great deal of modern technology depends on it.

Silicon is an essential element in biology, although only tiny traces of it appear to be required by animals. However, various sea sponges as well as microorganisms like diatoms and radiolaria secrete skeletal structures made of silica. Silica is often deposited in plant tissues, such as in the bark and wood of Chrysobalanaceae and the silica cells and silicified trichomes of Cannabis sativa, horsetails and many grasses.

2.2.1 Physical properties of Si:

Silicon is a solid at room temperature, with relatively high melting and boiling points of 1414 and 3265 °C, respectively. It has a greater density in a liquid state than a solid state. It does not contract when it freezes like most substances, but expands, similar to how ice is less dense than water. It has a relatively high thermal conductivity of 149 $W \cdot m^{-1} \cdot K^{-1}$, silicon conducts heat well and as a result is not often used to insulate hot objects.

In its crystalline form, pure silicon has a gray color and a metallic luster. Like germanium, silicon is rather strong, very brittle, and prone to chipping. Silicon, like carbon and germanium, crystallizes in a diamond cubic crystal structure, with a lattice spacing of 0.5430710 nm (5.430710 Å).

The outer electron orbital of silicon, like that of carbon, has four valence electrons. The 1*s*, 2*s*, 2*p* and 3*s* subshells are completely filled while the 3*p* subshell contains two electrons out of a possible six.

Silicon is a semiconductor. It has a negative temperature coefficient of resistance, since the number of free charge carriers increases with temperature. The electrical resistance of single crystal silicon significantly changes under the application of mechanical stress due to the piezoresistive effect. Table 2.6 below shows the physical properties of silicon.

Table 2.6 Physical properties of silicon

Properties	Value

Phase	solid
Melting point	1687 K, 1414 °C, 2577 °F
Boiling point	3538 K, 3265 °C, 5909 °F
Density (near r.t.)	2.3290 g·cm^{-3} (at 0 °C, 101.325 kPa)
Liquid density	at m.p.: 2.57 g·cm^{-3}
Heat of fusion	50.21 kJ·mol^{-1}
Heat of vaporization	383 kJ·mol^{-1}
Molar heat capacity	19.789 J·mol^{-1}·K^{-1}
Crystal structure	diamond cubic
Speed of sound	thin rod: 8433 m·s^{-1} (at 20 °C)
Thermal expansion	2.6 µm·m^{-1}·K^{-1} (at 25 °C)
Thermal conductivity	149 W·m^{-1}·K^{-1}
Electrical resistivity	at 20 °C: 10 Ω·m
Band gap	1.12 eV (at 300 K)
Magnetic ordering	diamagnetic
Young's modulus	130-188 GPa
Shear modulus	51-80 GPa
Bulk modulus	97.6 GPa
Poisson ratio	0.064 - 0.28
Mohs hardness	7
CAS Number	7440-21-3

2.2.2 Structure of Si:

Silicon has the same diamond cubic crystal structure as diamond, with each silicon atom covalently bonded in between four neighbors.

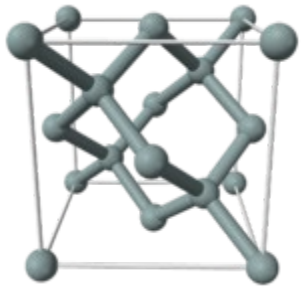

Figure 2.2: Silicon crystallizes in a diamond cubic crystal structure

Table 2.7 Vapor pressure of Silicon

P (Pa)	1	10	100	1 k	10 k	100 k
at T (K)	1908	2102	2339	2636	3021	3537

2.2.3 Chemical properties of Si:

Silicon is a metalloid, readily either donating or sharing its four outer electrons, allowing for many forms of chemical bonding. Like carbon, it

typically forms four bonds. Unlike carbon, it can accept additional electrons and form five or six bonds in a sometimes more labile silicate form. Tetra-valent silicon is relatively inert, but still reacts with halogens and dilute alkalis, but most acids (except for some hyper-reactive combinations of nitric acid and hydrofluoric acid) have no known effect on it. However, having four bonding electrons gives it, like carbon, many opportunities to combine with other elements or compounds in the right circumstances. Table 2.8 below shows the atomic properties.

Table 2.8 Atomic properties of Silicon

Properties	Value
Oxidation states	4, 3, 2, 1 −1, −2, −3, −4 (an amphoteric oxide)
Electronegativity	1.90 (Pauling scale)
Ionization energies	1st: 786.5 kJ·mol^{-1} 2nd: 1577.1 kJ·mol^{-1} 3rd: 3231.6 kJ·mol^{-1}
Atomic radius	empirical: 111 pm
Covalent radius	**2** pm

2.2.4 Applications of Silicon:

Most silicon is used industrially without being separated into the element, and indeed often with comparatively little processing from natural occurrence. Over 90% of the Earth's crust is composed of silicate minerals, which are compounds of silicon and oxygen, often with metallic ions when charged silicate anions require cations to balance charge. Many of these have direct commercial uses, such as clays, silica sand and most kinds of building stone. Thus, the vast majority of uses for silicon are as structural compounds, either as the silicate minerals or silica (crude silicon dioxide). For example, silica is an important part of ceramic brick. Silicates are used in making Portland cement which is used in building mortar and stucco, but more importantly combined with silica sand, and gravel (usually containing silicate minerals like granite), to make the concrete that is the basis of most of the very largest industrial building projects of the modern world.

Silicate minerals are also in white-ware ceramics, an important class of products usually containing various types of fired clay (natural aluminium silicate). An example is porcelain which is based on silicate mineral kaolinite. Ceramics include art objects, and domestic, industrial and building products. Traditional quartz-based soda-lime glass also functions in many of the same roles.

Very occasional elemental silicon is found in nature, and also naturally-occurring compounds of silicon and carbon (silicon carbide) or nitrogen (silicon nitride) are found in stardust samples or meteorites in presolar grains, but the oxidizing conditions of the inner planets of the solar system make planetary silicon compounds found there mostly silicates and silica.Free silicon, or compounds of silicon in which the element is covalently attached to hydrogen, boron, or elements other than oxygen, are mostly artificially produced. They are described below.

Silicon compounds of more modern origin function as high-technology abrasives and new high-strength ceramics based upon silicon carbide. Silicon is a component of some superalloys.

Alternating silicon-oxygen chains with hydrogen attached to the remaining silicon bonds form the ubiquitous silicon-based polymeric materials known as silicones. These compounds containing silicon-oxygen and occasionally silicon-carbon bonds have the capability to act as bonding intermediates between glass and organic compounds, and to form polymers with useful properties such as impermeability to water, flexibility and resistance to chemical attack. Silicones are often used in waterproofing treatments, molding compounds, mold-release agents, mechanical seals, high temperature greases and waxes, and caulking compounds. Silicone is also sometimes used in breast implants, contact lenses, explosives and pyrotechnics. Silly Putty was originally made by adding boric acid to silicone oil.

Alloys: Elemental silicon is added to molten cast iron as ferrosilicon or silicocalcium alloys to improve performance in casting thin sections and to prevent the formation of cementite where exposed to outside air. The presence of elemental silicon in molten iron acts as a sink for oxygen, so that the steel carbon content, which must be kept within narrow limits for each type of steel, can be more closely controlled. Ferrosilicon production and use is a monitor of the steel industry, and although this form of elemental silicon is grossly impure, it accounts for 80% of the world's use of free silicon. Silicon is an important constituent of electrical steel, modifying its resistivity and ferromagnetic properties.

The properties of silicon can be used to modify alloys with metals other than iron. "Metallurgical grade" silicon is silicon of 95–99% purity. About 55% of the world consumption of metallurgical purity silicon goes for production of aluminium-silicon alloys (silumin alloys) for aluminium part casts, mainly for use in the automotive industry. Silicon's importance in aluminium casting is that a significantly high amount (12%) of silicon in aluminium forms a eutectic mixture which solidifies with very little thermal contraction. This greatly reduces tearing and cracks formed from stress as

casting alloys cool to solidity. Silicon also significantly improves the hardness and thus wear-resistance of Aluminum.

Electronics: **Semiconductor device fabrication**, Since most elemental silicon produced remains as ferrosilicon alloy, only a relatively small amount (20%) of the elemental silicon produced is refined to metallurgical grade purity (a total of 1.3–1.5 million metric tons/year). The fraction of silicon metal which is further refined to semiconductor purity is estimated at only 15% of the world production of metallurgical grade silicon. However, the economic importance of this small very high-purity fraction (especially the ~ 5% which is processed to monocrystalline silicon for use in integrated circuits) is disproportionately large.

Pure monocrystalline silicon is used to produce silicon wafers used in the semiconductor industry, in electronics and in some high-cost and high-efficiency photovoltaic applications. In terms of charge conduction, pure silicon is an intrinsic semiconductor which means that unlike metals it conducts electron holes and electrons that may be released from atoms within the crystal by heat, and thus increase silicon's electrical conductivity with higher temperatures. Pure silicon has too low a conductivity (i.e., too high a resistivity) to be used as a circuit element in electronics. In practice, pure silicon is doped with small concentrations of certain other elements, a process that greatly increases its conductivity and adjusts its electrical response by controlling the number and charge (positive or negative) of activated carriers. Such control is necessary for transistors, solar cells, semiconductor detectors and other semiconductor devices, which are used in the computer industry and other technical applications. For example, in silicon photonics, silicon can be used as a continuous wave Raman laser medium to produce coherent light, though it is ineffective as an everyday light source.

In common integrated circuits, a wafer of monocrystalline silicon serves as a mechanical support for the circuits, which are created by doping, and insulated from each other by thin layers of silicon oxide, an insulator that is easily produced by exposing the element to oxygen under the proper conditions. Silicon has become the most popular material to build both high power semiconductors and integrated circuits. The reason is that silicon is the semiconductor that can withstand the highest temperatures and electrical powers without becoming dysfunctional due to avalanche breakdown (a process in which an electron avalanche is created by a chain reaction process whereby heat produces free electrons and holes, which in turn produce more current which produces more heat). In addition, the insulating oxide of silicon is not soluble in water, which gives it an advantage over germanium (an

element with similar properties which can also be used in semiconductor devices) in certain type of fabrication techniques.

Monocrystalline silicon is expensive to produce, and is usually only justified in production of integrated circuits, where tiny crystal imperfections can interfere with tiny circuit paths. For other uses, other types of pure silicon which do not exist as single crystals may be employed. These include hydrogenated amorphous silicon and upgraded metallurgical-grade silicon (UMG-Si) which are used in the production of low-cost, large-area electronics in applications such as liquid crystal displays, and of large-area, low-cost, thin-film solar cells. Such semiconductor grades of silicon which are either slightly less pure than those used in integrated circuits, or which are produced in polycrystalline rather than monocrystalline form, make up roughly similar amount of silicon as are produced for the monocrystalline silicon semiconductor industry, or 75,000 to 150,000 metric tons per year. However, production of such materials is growing more quickly than silicon for the integrated circuit market. By 2013 polycrystalline silicon production, used mostly in solar cells, is projected to reach 200,000 metric tons per year, while monocrystalline semiconductor silicon production (used in computer microchips) remains below 50,000 tons/year (Wikipedia, 2014).

2.3 Laser surface engineering

Surface modification is the act of modifying the surface of a material by bringing physical, chemical or biological characteristics different from the ones originally found on the surface of a material.

This modification is usually made to solid materials, but it is possible to find examples of the modification to the surface of specific liquids.

The modification can be done by different methods with a view to altering a wide range of characteristics of the surface, such as: roughness, hydrophilicity, surface charge, surface energy, biocompatibility and reactivity.

Surface engineering is the sub-discipline of materials science which deals with the surface of solid matter. It has applications to chemistry, mechanical engineering, and electrical engineering (particularly in relation to semiconductor manufacturing).

Solids are composed of a bulk material covered by a surface. The surface which bounds the bulk material is called the Surface phase. It acts as an interface to the surrounding environment. The bulk material in a solid is called the Bulk phase.

The surface phase of a solid interacts with the surrounding environment. This interaction can degrade the surface phase over time. Environmental degradation of the surface phase over time can be caused by wear, corrosion, fatigue and creep.

Surface engineering involves altering the properties of the Surface Phase in order to reduce the degradation over time. This is accomplished by making the surface robust to the environment in which it will be used (Wikipedia, 2014).

Surface patterning and texturing are becoming increasingly important for a wide range of applications. However, in order to bring these processes to industrial use easy-to-handle and cost effective microfabrication methods are required. Femtosecond lasers are powerful tools for this purpose, owing to their considerable advantages over long-pulse duration lasers. Due to their extremely short pulse duration, a very high peak power is achieved leading to intense non-linear effects. As a result, almost any type of material can be processed, including transparent dielectrics, polymers and metals, without undesirable collateral thermal effects (Oliveira, (2012).

2.3.1 Laser Direct Writing (LDW) Process:

From the earliest work on laser interactions with materials, direct-write processes have been important and relevant techniques to modify, add, and subtract materials for a wide variety of systems and for applications such as metal cutting and welding. In general, direct-write processing refers to any technique that is able to create a pattern on a surface or volume in a serial or “spot-by-spot” fashion. This is in contrast to lithography, stamping, directed self-assembly, or other patterning approaches that require masks or preexisting patterns.

At first glance, one may think that direct-write processes are slower or less important than these parallelized approaches. However, direct-write allows for precise control of material properties with high resolution and enables structures that are either impossible or impractical to make with traditional parallel techniques. Furthermore, with continuing developments in laser technology providing a decrease in cost and an increase in repetition rates, there is a plethora of applications for which laser direct-write (LDW) methods are a fast and competitive way to produce novel structures and devices (Craig & Alberto, 2007).

There are many types of direct-write techniques used in science and engineering. In the most classical sense, engraving or milling can be

considered a direct-write process, since a tool or stylus makes contact with a surface and is moved in a desired pattern to produce a feature. The coupling of a high powered laser with direct-write processing enables similar features to be produced without requiring physical contact between a tool and the material of interest. Because of this, few techniques share the versatility of LDW in adding, subtracting, and modifying different types of materials over many different length scales, from the nanometer to the millimeter scale. In LDW, the beam is typically focused or collimated to a small spot (in industrial processes, this “small” spot can be several millimeters in diameter). Patterning is achieved by either rastering the beam above a fixed surface or by moving the substrate or part within a fixed beam. An important feature of LDW is that the desired patterns can be constructed in both two and three dimensions on arbitrarily shaped surfaces, limited only by the degrees of freedom and resolution of the motion-control apparatus. In this manner, LDW can be considered a “rapid prototyping” tool (Piqué & Chrisey, 2002; Kai, Fai & Sing, 2004), because designs and patterns can be changed and immediately applied without the need to fabricate new masks or molds.

The key elements of any LDW system can be divided into three subsystems: (1) laser source, (2) beam delivery system, and (3) substrate/target mounting system (see Figure 2.3). At the heart of any LDW process is the laser source. Typical experiments and applications use anywhere from ultrafast femtosecond-pulsed systems to continuous-wave systems employing solid-state, gas, fiber, semiconductor, or other lasing media. In choosing an appropriate source, one must consider the fundamental interactions of lasers with the material of interest. This requires knowledge of the pulse duration, wavelength, divergence, and other spatial and temporal characteristics that determine the energy absorption and the material response. In beam delivery, there are a variety of ways to generate a laser spot, including fixed focusing objectives and mirrors, galvanometric scanners, optical fibers, or even fluidic methods such as liquid-core waveguides or water jets. The choice depends on the application demands, for instance, the required working distances, the focus spot size, or the energy required. The ultimate beam properties will be determined by the combination of laser and beam delivery optics. Finally, the substrate mounting is done in accordance with experimental or industrial requirements and can be manipulated in multiple directions to achieve a desired result. Robotics and active feedback control, on either the substrate or beam delivery optics, can add further design flexibility to the technique.

There is a vast range of LDW processes. For the purposes of this issue, we categorize them into three main classes: laser direct write subtraction (LDW-), here material is removed by ablation; laser direct-write modification (LDWM), where material is modified to produce a desired effect; and laser direct-write addition (LDW+), where material is added by the laser.

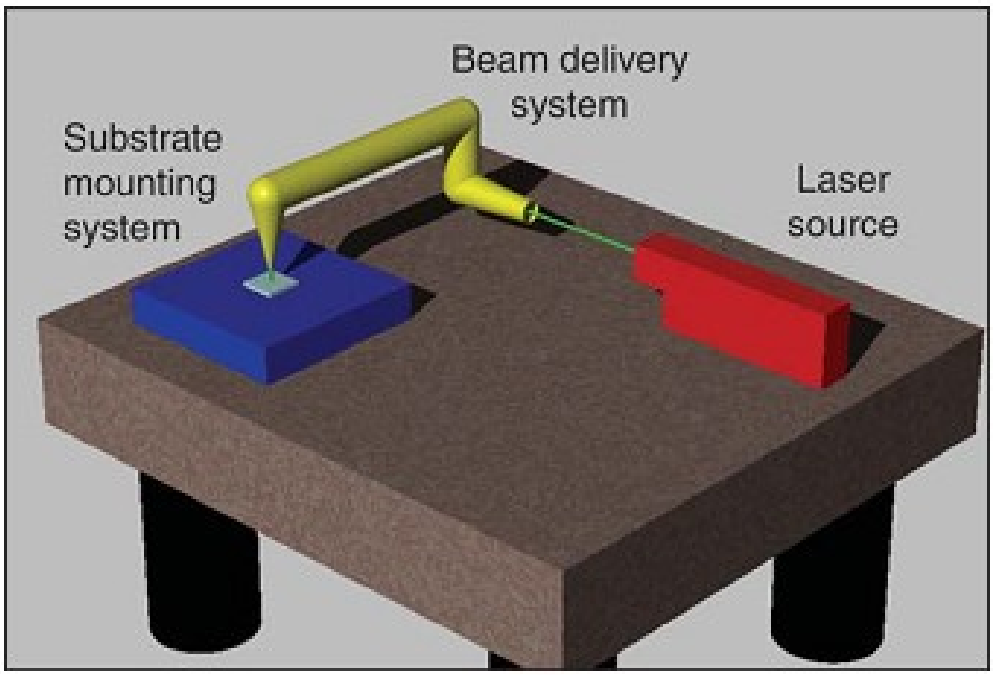

Figure 2.3: Schematic illustration of a laser direct-write system.

2.3.1.1 Laser Direct-Write Subtraction (LDW–):

LDW– is the most common type of laser direct-write. In general, this entails processes that result in photochemical, photothermal, or photophysical ablation on a substrate or target surface, directly leading to the features of interest. Common processes include laser scribing, cutting, drilling, or etching to produce relief structures or holes in materials in ambient or controlled atmospheres. Industrial applications using this technique range from high-throughput steel fabrication, to inkjet and fuel-injection nozzle fabrication, to high-resolution manufacturing and texturing of stents or other implantable biomaterials. At a smaller scale, inexpensive bench-top laser cutting and engraving systems can be purchased by the hobbyist or small company for artistic and architectural renderings. More recent developments in LDW include chemically assisted techniques such as laser-drilling ceramics or biomaterials and laser-induced backside wet etching (LIBWE) of glass (Ding et al., 2002, p. 641; Kopitkovas et al., 2003, p. 438). In fact, one may also consider laser cleaning to be a controlled LDW–process.

The fundamental interactions leading to material removal can be thermal or athermal, depending primarily on the material/environment characteristics and the pulse duration of the laser. These interactions have a direct effect on the quality of the resulting features. For instance, a heat affected zone (HAZ) tends to occur in the vicinity of thermally removed material. This region has structures and properties that can differ from the bulk material and can exhibit additional surface relief. Either of these effects may be beneficial or detrimental, depending on the application. In contrast, athermal and multiphoton absorption processes caused by ultrafast lasers can reduce the formation of a HAZ and enable features smaller than the diffraction limit (Pronko et al., 1995, p. 106; Lenzner et al, 1999, p. 369).

2.3.1.2 Laser Direct-Write Modification (LDWM):

In LDWM, the incident laser energy is usually not sufficient to cause ablative effects but is sufficient to cause a permanent change in the material properties. Typically, these processes rely on thermal modifications that cause a structural or chemical change in the material. A common example of such processes is the rewritable compact disc, in which a diode laser induces a phase transition between crystalline and amorphous material. In industrial applications, one may consider laser cladding, where a surface layer different from the bulk material is produced through melting and resolidification, or solid free-form fabrication (SFF) approaches such as selective laser sintering (SLS), as important modifying processes that would fall under the umbrella of LDWM.

Many LDWM applications require a specific optical response in the material of interest beyond simple thermal effects. Optically induced defects or changes in mechanical properties can lead to many non-ablative material modifications. For instance, photoresists respond to light by breaking or reforming bonds, leading to pattern formation in the material. Alternatively, LDW can cause defects in photoetchable glass ceramics or other optical materials through single- and multiphoton mechanisms, enabling novel applications in optical storage, photonic devices, and microfluidics.

2.3.1.3 Laser Direct-Write Addition (LDW+):

LDW+ is perhaps the most recent of the laser direct-write processes. In this technique, material is added to a substrate using various laser-induced processes. Many techniques are derived from laser induced forward transfer (LIFT), where a sacrificial substrate of solid metal is positioned in close proximity to a second substrate to receive the removed material. The incident

laser is absorbed by the material of interest, causing local evaporation. This vapor is propelled toward the waiting substrate, where it re-condenses as an individual three-dimensional pixel, or voxel, of solid material. Such an approach has found important use in circuit and mask repair and other small-scale applications where one needs to deposit material locally to add value to an existing structure. This general technique has significant advantages over other additive direct-write processes, in that these laser approaches do not require contact between the depositing material and a nozzle, and can enable a broad range of materials to be transferred. Variations on the general LIFT principle allow liquids, inks, and multiphase solutions to be patterned with computer-controlled accuracy for use in a variety of applications such as passive electronics or sensors (Chrisey et al, 2000, p. 593; Pique et al, 2003, p. 293).

Alternatively, LDW+ techniques can rely on optical forces to push particles or clusters into precise positions, or on chemical changes in liquids and gases to produce patterns. For instance, laser-induced chemical vapor deposition, or multiphoton polymerization schemes of liquid photoresists, can be used to fabricate three-dimensional stereographic patterns. Examples of this have been demonstrated and show promise for many applications such as fabricating photonic structures or biological scaffolding.

Direct laser structuring of materials has been successfully employed in fields of micro-fabrication for over a decade. Recently, the trend in laser micro-fabrication of materials has been moving from two-dimensional surface modifications towards three-dimensional volumetric structuring, responding to demands for higher-order integration. Femtosecond laser direct writing provides a unique means of volumetric processing with nanometer precision. Since it is based on multi-photon absorption processes, it allows the fabrication of three-dimensional structures within a transparent medium without degradation of the surface quality (Craig & Alberto, 2007).

2.3.2 Lasers for materials processing:

Lasers, with their unique coherent, monochromatic, and collimated beamy characteristics, are used in ever-expanding fields of applications. Different applications require laser beams of different pulse duration and output power. Lasers employed for materials processing range from those with a high peak power and extremely short pulse duration to lasers with high-energy continuous-wave output.

2.3.2.1 Continuous-wave – millisecond – microsecond lasers

Continuous-wave (CW) and long-pulsed lasers are typically used to process materials either at a fixed spot (penetration material removal) or in a scanning mode whereby either the beam or the target is translated. Millisecond- and microsecond-duration pulses are produced by chopping the CW laser beam or by applying an external modulated control voltage. Fixed Q-switched solid-state lasers with pulse durations from tens of microseconds to several milliseconds are often used in industrial welding and drilling applications. Continuous-wave carbon dioxide lasers (wavelength λ = 10.6 μm and power in the kilowatt range) are widely employed for the cutting of bulk and thick samples of ceramics such as SiN, SiC, and metal-matrix ceramics (e.g. Duley, 1983). Continuous-wave laser radiation allows definition of grooves and cuts. On the other hand, low-power CO_2 lasers in the 10–150-W range are used for marking of wood, plastics, and glasses. Argon-ion lasers operating in the visible range (λ=419–514 nm) are utilized for trimming of thick and thin resistors. In the biomedical field various CW lasers have been used. For example, the CO_2 laser radiation is absorbed in the tissue within a layer of depth about 20 m, thus achieving a continuous ablation front. On the other hand, the Nd: YAG (λ=1064 nm) and argon-ion radiation penetration is of the order of millimeters, giving rise to explosive ablation events. Srinivasan et al.(1995) used an argon-ion laser operating in the UV ranges of 275–305 and 350–380 nm to ablate polyimide Kapton films. By chopping the laser beam to produce millisecond and microsecond pulses, they showed that the ablation process scales with an intensity threshold rather than the commonly used threshold. This is certainly not surprising, since, if the laser energy is spread over a long pulse, the beam intensity weakens and the induced temperature and structural and chemical response of the target may be of different nature.

In fact, Srinivasan (1992) showed that the etching of polymer films with long, millisecond–microsecond pulses leaves evidence of molten material and carbonization of the walls, although not indicative of the ablation process that characterizes nanosecond-pulse UV laser ablation. Microfabrication applications involving direct writing can be effected by CW Ar^+ and Kr^+ lasers, utilizing frequency-doubled lines. Highpower CW Nd : YAG lasers operating on the fundamental wavelength and on frequencydoubled and -tripled harmonics are often used for various cutting and microprocessing applications (Costas,2009, pp.33-34).

2.3.2.2 Femtosecond lasers

Femtosecond laser micromachining has become increasingly important in recent years for many fields, including micro-optics, micro-electronics, micro-biology, and micro-chemistry. Laser ablation, because of its non-contact nature, allows the micromachining and surface patterning of materials with minimal mechanical and thermal deformation. It is now well known that for many of these applications, the femtosecond regime offers advantages over the nanosecond regime. These advantages lie in its ability to deposit energy into a material in a very short time period, before thermal diffusion can occur. As a result, the heat-affected zone, where melting and solidification can occur, is significantly reduced. Smaller feature sizes, greater spatial resolution, and better aspect ratios can hence be achieved.

Another advantage of femtosecond laser micromachining is its versatility in terms of both the materials that can be processed and the type of processing. A variety of materials have been demonstrated to be suitable for femtosecond laser micromachining, such as metals, semiconductors, polymers, oxide ceramics, silica aerogels, optical glasses, and crystals. A variety of processing methods have been used, including the fabrication of photonic crystals, waveguides, gratings and single mode couplers, and the storage of data (Zoubir et al., 2003, p.311).

In the sub-picosecond or femtosecond regime, the laser pulse is shorter than the relaxation times, and the equilibrium assumption is no longer valid, necessitating treatment of the microscopic mechanisms of energy transfer via quantum mechanics. One notable characteristic of femtosecond lasers is the high radiation intensity that has the ability to create high-density plasmas. On the other hand, by beating the thermal diffusion time scale, femtosecond-laser radiation can in principle be used for micromachining with minimal thermal damage to the surrounding area. In the UV range, KrF (λ=248 nm) excimer lasers with typical pulse duration 500 fs and pulse energies in the range several to tens of millijoules have been demonstrated in the processing of Al and glassy C (Sauerbrey et al., 1994), Ni, Cu, Mo, In, Au, W (Preuss et al., 1995), fused silica (Ihlemann, 1992), and ceramics such as Al_2O_3, MgO, and ZrO_2(Ihlemann et al., 1995), and for polymer ablation (Boret al.,1995; Wolff-Rottke et al.,1995). KrF excimer lasers have also been used in studies of high-density-gradient Al and Au plasmas (Fedosejevs et al., 1990) and for production of soft X-rays from Al (Teubner et al., 1993). The latter was also accomplished from Cu and Ta targets by near-IR Ti : sapphire-laser irradiation at λ=807 nm, with pulse duration 120 fs and pulse energy 60 mJ (Kmetec et al., 1992). A Ti: sapphire system with pulse duration of 150 fs andλ=770 nm was used in studies of gold ablation (Pronko et al., 1995), while pulse durations of 170–200 fs at wavelength λ = 798 nm and energy 4 mJ ablated

polymers through a multiphoton ablation mechanism. Ti: sapphire-laser technology is often utilized in the laboratory environment and has recently made inroads into industrial applications, for example in the repair of lithographic masks. Amplified systems typically deliver 1-mJ near-IR pulses at maximum frequency 1 kHz. By utilizing stronger pumping lasers it is possible to extract pulses in the range tens of millijoules, albeit at reduced frequencies. On the other hand, the laser system could be configured to deliver microjoule or picojoule pulses at higher frequencies. Intense, visible dye-laser radiation (pulse duration 160 fs, λ=616 nm, energy 5 mJ) generated Si plasmas of high-energy-X-ray-emitting density (Murnane et al., 1989). In a biomedical application (Kautek et al., 1994), a dye laser (pulse duration 300 fs, λ=615 nm, pulse energy > 0.18 mJ) produced high-quality ablation in human corneas, characterized by damage zones less than 0.5m wide. An interesting development in high-repetition-rate femtosecond-laser systems has been the development of (fiber) lasers that may give Megahertz repetition rates with hundreds of nanojoules per pulse or correspondingly pulse rates of∼100 kHz at tens of microjoules per pulse at λ=1,064 nm with pulse duration∼200 fs. Similar specifications have been achieved with disk or directly diode-pumped high-energy femtosecond oscillators. These lasers are utilized for film micromachining and the internal writing of optical waveguide structures in transparent materials (Costas, 2009, p. 36).

2.3.3 LDW Laser Sources:

Lasers used for LDW processes in this work are the Diode Laser and the titanium–sapphire (Ti: sapphire) laser.

2.3.3.1 The diode laser:

A diode, laser operates in the near-infrared and into the visible region of the spectrum. Like the ruby and Nd^{3+}:YAG lasers it is a solid state laser but the mechanism involved is quite different.

Figure 2.4 (a) shows how the conduction band C and the empty valence band V are not separated in a conductor whereas Figure 2.4(c) shows that they are well separated in an insulator. The situation in a semiconductor, shown in Figure 2.4(b), is that the band gap, between the conduction and valence bands, is sufficiently small that promotion of electrons into the conduction band is possible by heating the material. For a semiconductor the Fermi energy E_F, such that at T = 0 K all levels with $E < E_F$ are filled, lies between the bands.

Semiconductors may also be made from a material which is normally an insulator by introducing an impurity, a process known as doping. Figure 2.5 shows two ways in which an impurity may promote semiconducting properties. In Figure 2.5(a) the dopant has one more valence electron per atom than the host and contributes a band of filled impurity levels I close to the conduction band of the host. This characterizes an n-type semiconductor. An example is silicon ($KL3s^2 3p^2$) doped with phosphorus ($KL3s^2 3p^3$) , which reduces the band gap to about 0.05 eV. Since kT at room temperature is about 0.025 eV, the phosphorus converts silicon from a high-temperature semiconductor into a room-temperature semiconductor.

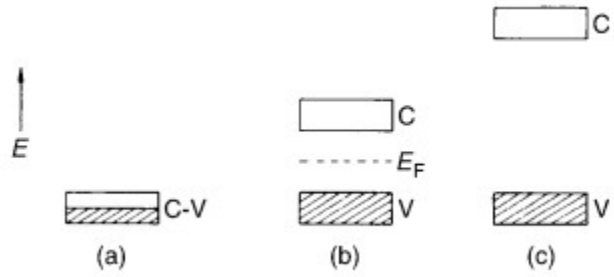

Figure 2.4: Conduction band, C, and valence band, V, in (a) a conductor, (b) a semiconductor and (c) an insulator

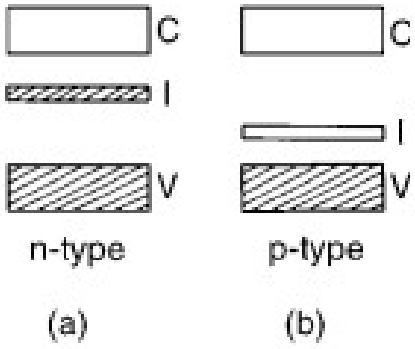

Figure 2.5: Impurity levels I in (a) an n-type and (b) a p-type semiconductor; C is the conduction band and V the valence band

Alternatively, as in Figure 2.5(b), a doping with one valence electron fewer than the host contributes an impurity band I which is empty but more accessible to electrons from the valence band. An example of such a p-type semiconductor is silicon doped with aluminium ($KL3s^2 3p^1$) in which the band gap is about 0.08 eV.

A semiconductor laser takes advantage of the properties of a junction between a p-type and an n-type semiconductor made from the same host material. Such an n–p combination is called a semiconductor diode. Doping concentrations are quite high and, as a result, the conduction and valence band energies of the host are shifted in the two semiconductors, as shown in Figure 2.6(a). Bands are filled up to the Fermi level with energy E_F. If a voltage is applied to the junction with the negative and positive terminals attached to the n and p regions, respectively, electrons flow from the n to the p region, and positive holes in the opposite direction. The levels are also displaced, as shown in Figure 2.6(b) and the Fermi energies E'_F(n) and E''_F(p) are now unequal, resulting in a population inversion in the region of the junction and leading to laser action. The semiconductor laser is, unusually, an example of a two-level system, but the population inversion is not obtained by pumping.

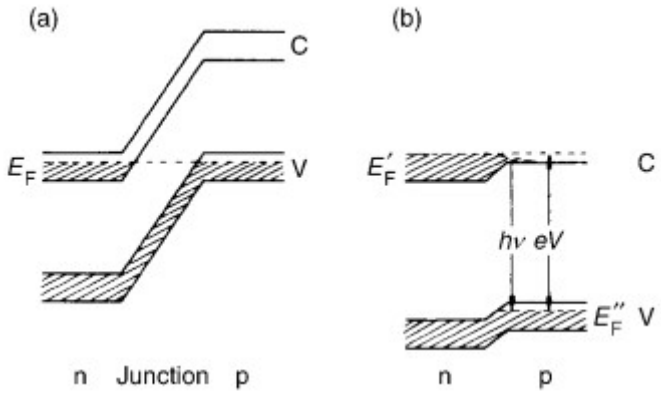

Figure 2.6: (a) The Fermi level E_F in the region of a p–n junction. (b) The result of applying a voltage across the junction; C is the conduction band and V the valence band

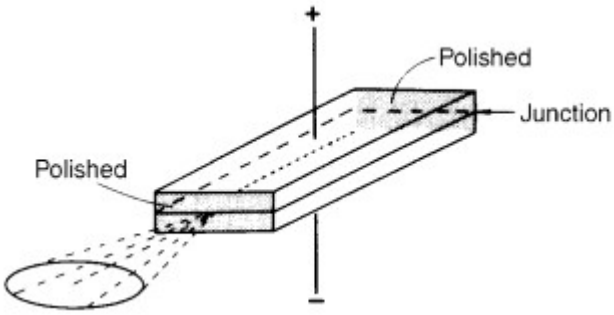

Figure 2.7: Diode, laser

A typical semiconductor laser, shown in Figure 2.7, is small, only a few millimeters long and with an effective thickness of about 2mm.

A variety of materials are used depending on the region in which the laser is required to operate. For example, a range of lead alloy semiconductors

such as $Pb_{1-x}Sn_xSe$ and PbS_{1-x} Se_x covers the range 2.8–30mm. Semiconductor lasers can be tuned but the tuning range of a particular laser is small so that a whole series of them is necessary to cover an appreciable wavelength range. Gross tuning of the wavelength is achieved by surrounding the laser with a refrigeration unit to control and vary the temperature.

The two ends of the laser diode in Figure 2.7 are polished to increase internal reflection. As a consequence of the cavity geometry the laser beam is, unlike that of most lasers, highly divergent.

Semiconductor lasers are some of the most efficient of all lasers, with an efficiency of about 30 per cent (Hollas, 2004, pp. 350-352).

2.3.5.2 The titanium–sapphire (Ti: sapphire) laser:

Despite the fact that the first laser to be produced (the ruby laser) has the remarkable property of having all its power concentrated into one or two wavelengths, a property possessed by most lasers, it was soon realized that the inability to change these wavelengths appreciably, that is to tune the laser, is a serious drawback which limits the range of possible applications.

Historically, the first type of laser to be tunable over an appreciable wavelength range was the dye laser. The alexandrite laser, a tunable solid state laser, was first demonstrated in 1978 and then, in 1982, the titanium– sapphire laser. This is also a solid state laser but tunable over a larger wavelength range, 670–1100 nm, than the alexandrite laser, which has a range of 720–800 nm.

The lasing medium in the titanium–sapphire laser is crystalline sapphire (Al_2O_3) with about 0.1 per cent by weight of Ti_2O_3. The titanium is present as Ti^{3+} and it is between energy levels of this ion that lasing occurs.

The ground configuration of Ti^{3+} is $KL3s^23p^63d^1$. The crystal field experienced by the ion splits the 3*d* orbital into a triply degenerate lower-energy t_2 orbital and a doubly degenerate higher-energy *e* orbital. If the electron is in the lower orbital a $^2T_2$ ground state results and, if it is in the upper orbital, a ^2E excited state results. These states are about 19 000 cm^{-1} apart but each is split into further components and is also coupled to the vibrations of the crystal lattice. In a similar way to that in alexandrite population inversion can be created between these two sets of levels resulting in a four-level vibronic laser with a tunable range of 670–1100 nm.

A further advantage, compared with the alexandrite laser, apart from a wider tuning range, is that it can operate in the CW as well as in the pulsed mode. In the CW mode the Ti $^{3+}$ – sapphire laser may be pumped by a CW argon ion laser and is capable of producing an output power of 5 W. In the pulsed mode pumping is usually achieved by a pulsed Nd^{3+}: YAG laser and a pulse energy of 100 mJ may be achieved.

In 1991 a remarkable discovery was made, accidentally, with a Ti^{3+} –sapphire laser pumped with an Ar+ laser. Whereas we would expect this to result in CW laser action, when a sharp jolt was given to the table supporting the laser, mode locking occurred. This is known as self-locking of modes, and we shall not discuss further the reasons for this and how it can be controlled. One very important property of the resulting pulses is that they are very short. Pulse widths of a few tens of femtoseconds can be produced routinely and with high pulse-to-pulse stability. Further modification to the laser can produce pulses as short a 8 fs. Commercially, such lasers are available producing pulse widths of less than 100 fs at a repetition rate of 80 MHz with a peak power of 1 W (Hollas, 2004, pp. 348-349).

2.4 Laser Interaction with Silicon and PMMA:

2.4.1 Ultrafast-laser interactions with materials:

Lasers that can produce coherent photon pulses with durations in the femtosecond regime have opened up new frontiers in materials research with extremely short temporal resolution and high photon intensity. The ultrafast nature of femtosecond lasers has been used to observe, in real time, phenomena including chemical reactions in gases (Zewail,1994) and electron–lattice energy transfer in solids (Shah, 1996). On the other hand, ultra-short laser pulses impart extremely high intensities and provide precise laser-ablation thresholds at substantially reduced laser energy densities. The increasing availability of intense femtosecond lasers has sparked a growing interest in high-precision materials processing. In contrast to material modification using nanosecond or longer laser pulses, for which standard modes of thermal processes dominate, there is no heat exchange between the pulse and the material during femtosecond-laser–material interactions. As a consequence, femtosecond laser pulses can induce nonthermal structural changes driven directly by electronic excitation and associated nonlinear processes, before the material lattice has equilibrated with the excited carriers. This fast mode of material modification can result in vanishing thermal stress and minimal collateral damage for processing practically any solid-state

material. Additionally, damage produced by femtosecond laser pulses is far more regular from shot to shot. These breakdown characteristics make femtosecond lasers ideal tools for precision material processing. Thorough knowledge of the short-pulse-laser interaction with the target material is essential for controlling the resulting modification of the target's topography. The use of ultra-short pulses with correspondingly high laser intensities reduces the extent of heat diffusion into the target, facilitating instantaneous material expulsion. This enables high-aspect-ratio cuts and features, free of debris and lateral damage (e.g. Momma et al., 1998; Pronko et al., 1995;Liu et al., 1997;Wu,1997). Therefore, the ablation process is stable and reproducible. As a result, the produced structure size is not limited by thermal or mechanical damage, i.e. melting, formation of burr and cracks, etc. Thus, the minimal achievable structure size is limited mainly by diffraction to the order of a wavelength (Korte et al., 1999). It has also to be recognized that ultrafast-laser pulses enforce high intensities that trigger nonlinear absorption effects that may dominate the interaction process. One of the most important repercussions is the efficient processings of transparent dielectrics, which has a number of applications, enabling for example three-dimensional binary-data storage (Glezer et al.,1996).

2.4.1.1 Femtosecond-laser interaction with semiconductor materials:

Depending on how the incident photon energy, $h\nu$, compares with the band gap, E_{bg}, absorption of ultra-short-pulse radiation takes place via single-photon and/or multiphoton interband absorption or free-carrier, intraband absorption. Interband absorption creates electron–hole pairs with an initial kinetic energy of $h\nu - E_{bg}$, whereas free-carrier absorption events endow the free carriers with an additional kinetic energy, $h\nu$. On a time scale that is less than 100 fs, the carriers thermalize to a Fermi–Dirac distribution via carrier–carrier collisions. Recombination and impact-ionization processes allow this thermalization to equilibrium number-density distributions. For the relevant carrier densities, $N > 10^{18}$ cm^{-3}, the dominant recombination process is Auger recombination, a three-body interaction process, whereby two carriers interact with a third carrier, increasing the electron temperature, T_e, but reducing the carrier number density, N. The impact-ionization process occurs when an energetic carrier creates an electron–hole pair while losing energy. The carriers then attempt to reach thermal equilibrium with the lattice, initially by emitting longitudinal-optical (LO) phonons. The carrier-LO relaxation time, τe, depends both on carrier temperature and on lattice

temperature. However, for silicon it is approximated as constant at 0.5 ps (Van Driel,1987). The LO phonon population attempts to thermalize with other lattice modes through phonon–phonon interaction. Even though some phonon modes might not attain thermal equilibrium until longer times, most of the deposited laser energy will be converted into a near-thermal equilibrium lattice state within times of order tens of picoseconds. The dominant interband absorption mechanism under short-pulse excitation is two-photon absorption as opposed to long-pulse irradiation since the one-photon absorption length is nearly 10μm in bulk, crystalline silicon and the probability of nonlinear processes increases with increasing intensity. The two-photon absorption coefficient, β (cm/GW), is given by Van Stryland et al.(1985):

$$\beta = (3.1\pm0.5)\times10^3\ [\sqrt{E}_p F_2(2h\nu/E_{bg})/n^2E^3_{bg}]\ , \qquad (2.1)$$

where E_p (eV) is a nearly material-independent constant, E_{bg} (eV) is the semiconductor bandgap, n is the real part of the complex refractive index, and F_2 is a function defined in Van Stryland et al.(1985) that is determined utilizing band-structure considerations.

The assumption of local quasi-equilibrium implies that the electron distribution follows the Fermi–Dirac function. The particle number density, electron energy, and lattice energy are then calculated via the relaxation time approximation to Boltzmann's transport equation. Given the short pulse duration (0.1 ps) relative to the electron–lattice relaxation time (∼0.5 ps), the relaxation-time approximation has limitations. Nevertheless, a qualitative description of the thermal and nonthermal heating processes can be established. Assuming that the quasi-Fermi level remains in the middle of the band gap, ignoring band-gap shrinkage according to temperature variation, and considering both linear and two-photon absorption, the balance equation for energy carriers can be written as follows:

$$\partial N/\partial t+\nabla\cdot(-D_0\nabla N)=[(1-R)\gamma I(x,t)/h\nu] + [(1-R)^2\beta I^2(x,t)/2h\nu] -\gamma_{Aug}N^3 + \delta(T_e)N, \qquad (2.2)$$

Where R is the reflectivity, γ is the linear absorption coefficient, β is the two-photon absorption coefficient, D_0 is the ambipolar diffusivity, $h\nu$ is the photon energy quantum, γ_{Aug} is the Auger-recombination coefficient, and δ is the impact-ionization coefficient. The gradient of the laser-beam intensity is then written as follows:

$$dI/dx = -\gamma I -\beta I^2 - \Theta NI\ , \qquad (2.3)$$

where Θ is the free-carrier absorption coefficient. The total energy-balance equations for the electron and lattice systems using the relaxation-time approximation can be written as follows:

$$\partial U_e/\partial t + \nabla\cdot(-k_e\nabla T_e) = (1-R)(\alpha+N)I(x,t) + (1-R)^2\beta^2 I^2(x,t) - G_e(T_e-Tl), \quad (2.4a)$$

$$\partial U_l/\partial t + \nabla\cdot(-k_l \nabla T_l) = G_e(T_e-T_l), \quad (2.4b)$$

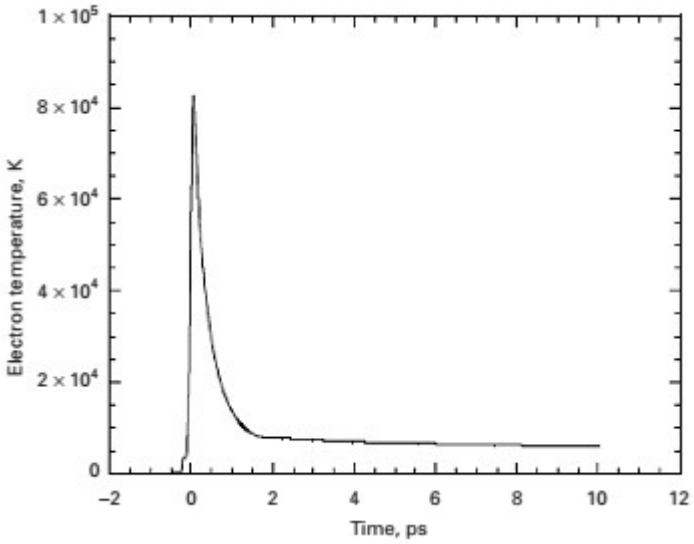

Figure 2.8 Evolution of the electron temperature in c-Si under irradiation by a 100-fs, 800-nm laser pulse of fluence F=1.5 J/cm^2.

Where U_e is the electron energy ($NE_g + \frac{3}{2}Nk_BT_e$) and U_l is the acoustic-phonon energy (C_lT_l). Ge is for the optical phonon and acoustic phonon (C_l/τ_l), respectively. The impact-ionization and Auger-recombination terms do not explicitly represent energy source or loss terms, since they both conserve energy. Figure 2.7 shows the evolution of the surface electron temperature upon irradiation of a crystalline silicon target by a femtosecond laser pulse of fluence F = 1.5 J/cm^2 and wavelength λ = 800 nm (Choi and Grigoropoulos,2002). Evidently, the electrons instantaneously absorb the laser energy, producing a very rapid increase of T_e. The corresponding lattice temperature is shown in Figure 2.9. If one were to trace the isotherm corresponding to the equilibrium melting point, T_m=1685 K, then the melt depth would reach 0.2–0.3μm within 10 ps. Assuming motion of a distinct phasetransition boundary, the corresponding interfacial speed would be of the order of 10^4 m/s. This exceeds by far any kinetic considerations linking interfacial speed to departures from the equilibrium melting point.

Consequently, the phase-transition process has to be extremely rapid and may evolve through a process fundamentally different from thermal melting.

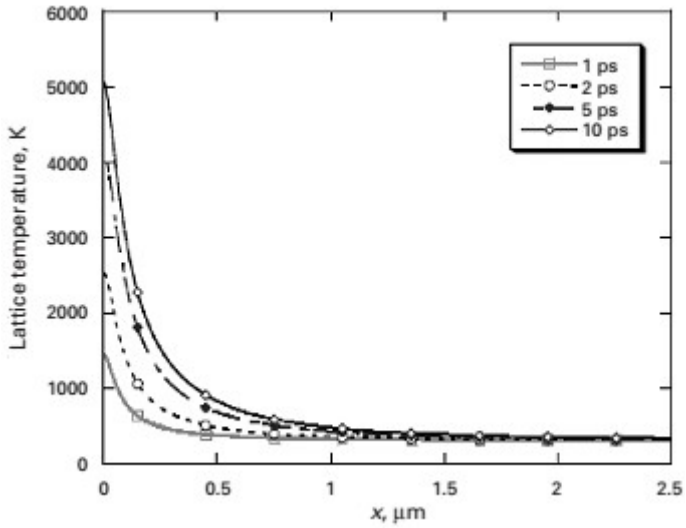

Figure 2.9: **Lattice temperature in c-Si under irradiation by a 100-fs, 800-nm laser pulse of fluence F=1.5 J/cm^2.**

2.4.1.2 Phase transformations induced by femtosecond laser irradiation

Crystalline silicon irradiation induces transformations like melting and ablation:

2.4.1.2.1 Melting of crystalline silicon

In an attempt to explain the laser annealing of crystal damage in ion-implanted semiconductors, Van Vechten et al. (1979) introduced the idea of plasma annealing, whereby the high-density electron plasma induces softening of the crystal lattice. The studies by Shank et al. (1983) and Downer et al.(1985) via time-resolved pump-and-probe surface-reflectivity measurement were the first to clearly show ultrafast phase change after an elapsed time of less than 1 ps. The nature of this phase change was discussed in terms of the Lindemann criterion (Ziman, 1964), whereby melting is considered to occur when the root-mean-square displacement of each atom is a fraction of the dimension of the unit cell (about 0.2–0.25 for most solids). Second-harmonic-generation (SHG) experiments showed that a c-Si sample irradiated by laser pulses of duration 75 ns at fluence of 0.2 J/cm^2 (i.e. twice the threshold fluence) underwent rapid phase change within a time of 150 fs. The optical properties of the top 75–130-nm-thick layer were found to reach those of molten silicon. As detailed by Sokolowski-Tinten et al.(1995), for laser fluences up to about 1.3 times the respective threshold fluence, structural transformation occurs on a time scale of several tens of picoseconds. This

rather slow phase transformation was attributed to thermal melting driven by the increase in lattice temperature. A fundamentally different type of phase transformation occurs for laser fluences exceeding 2–3 times the threshold fluence, whereby the material undergoes a direct transition to the liquid state within a few hundred nanoseconds.

Figure 2.10 shows an experimental setup for the in *situ* imaging of the surface reflectivity upon excitation by a laser pulse of duration 120 fs and wavelength 620 nm. The ultrafast-melting threshold for these laser-pulse parameters is at F_m=0.17J/cm^2.

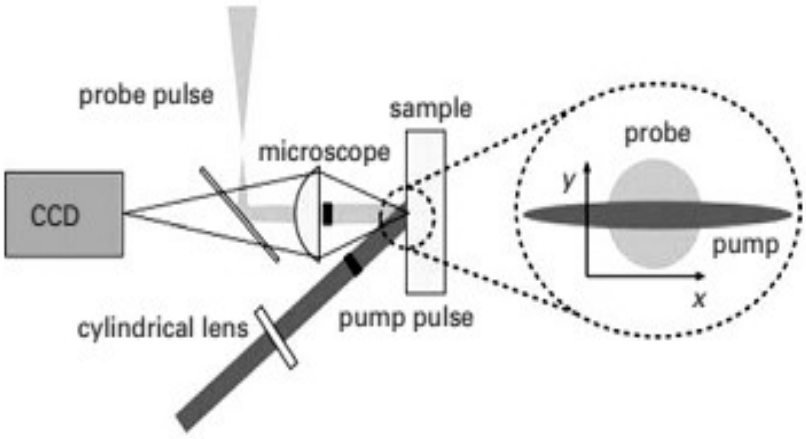

Figure 2.10: Left: a schematic diagram of the experimental setup. Right: an expanded view of the surface. Light and dark gray mark the areas covered by the probe and the pump, respectively.

The reflectivity traces obtained for a fluence about five times this threshold fluence indicate that the reflectivity initially drops but is eventually capped by the reflectivity corresponding to the liquid-silicon phase (Figure 2.11). These fluence dependences have been obtained from vertical cross sections of the picture shown on top, as marked by three vertical lines.

Since this process is faster than the characteristic electron–lattice relaxation time, it cannot possibly be ascribed to thermal processes. The generation of the high-density electron–hole plasma (of electron–hole number density higher than 10^{22}cm^{-3}) is a precursor to the observed phase transition and has been studied in detail by Sokolowski-Tinten and von der Linde (2000).

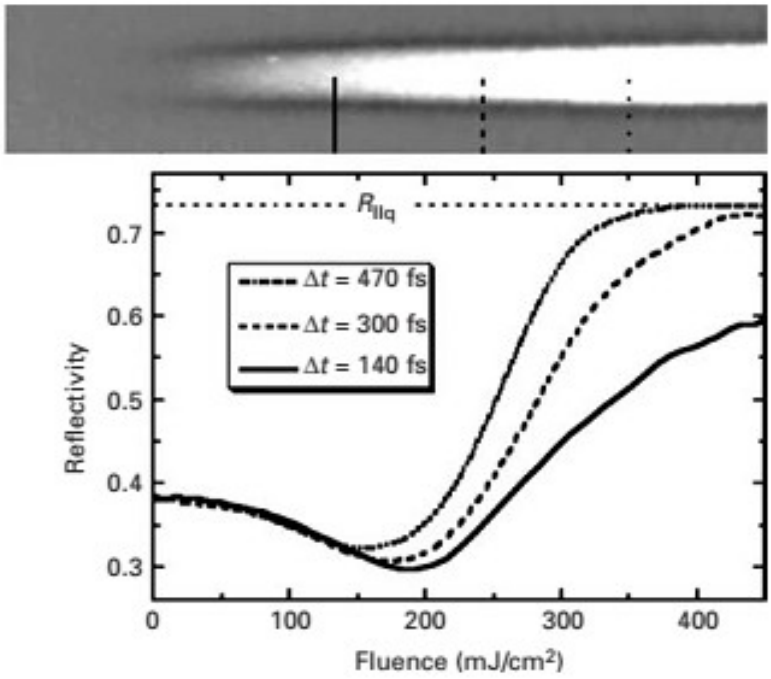

Figure: 2.11 The reflectivity of silicon as a function of the pump fluence for three different delay times between pump and probe.

The dielectric function of an optically excited semiconductor is

$$\varepsilon^*(h\nu) = 1+ [\varepsilon_g(h\nu + \Delta E_{bg}) -1] [N_0 - N_{e-h}] / [N_0]$$

$$- [N_{e-h} e^2] / [\varepsilon 0 m^*_{opt} m_e (2\pi\nu)^2][1] / [1+i/(2\pi\nu\tau_{Drude})] \quad , \quad (2.5)$$

$$m^*_{opt} = [1/ m^*_e] + [1/m^*_h]. \quad (2.6)$$

In the above equations, ε_g is the dielectric constant of the unexcited material, N_{e-h} is the density of the excited electron–hole pairs, N_0 is the total valence-band density in the unexcited state, m^*_{opt} is the effective mass of the carriers, m^*_e and m^*_h are the mobility effective masses of electrons and holes, respectively, and τ_{Drude} is the Dude damping time. The first two terms on the right-hand side of (2.5) account for state and band filling hand band-structure renormalization, while the last term quantifies the Drude contribution of the free carriers. While at low densities τ_{Drude} is determined by carrier– phonon scattering and is of the order of 100 fs, it drops at high densities, for which carrier–carrier collisions are important. Although both m^*_{opt} and τ_{Drude} do in principle depend on temperature, the optical response at high densities is dominated by free-carrier effects and well described by the Drude model. By fitting experimental reflectivity data to predictions, Sokolowski and von der

Linde (2000) inferred the optical effective mass $m^{*}opt$ = 0.18, the relaxation time τ_{Drude} = 1.1 fs, and the two-photon-absorption coefficient at 625 nm β = 5 0±10 cm/GW. Furthermore, the critical density for transition to ultrafast phase transition was about 10^{22} cm^{-3}. Figure 2.12 gives the electron–hole density as a function of the laser fluence derived from experimental data, together with the numerical predictions.

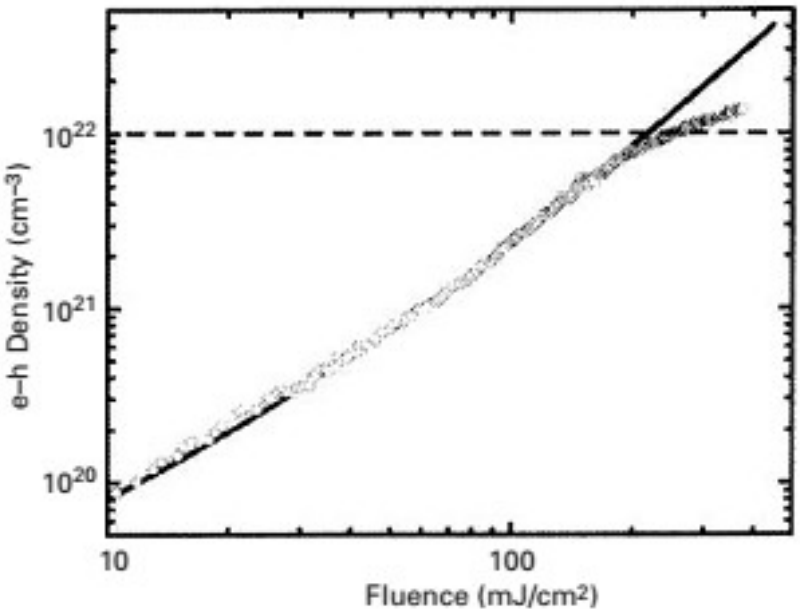

Figure 2.12: The absolute electron–hole density as a function of excitation fluence. Open circles: measured data points. Solid line: corrected density (taken from numerical simulations) to account for the steep spatial carrier distributions. The dashed line marks a threshold density of $10^{22}cm^{-3}$.

Theoretical studies have also been performed to assess the mechanisms of the ultrafast "plasma-annealing" and phase-transformation processes. Theoretical studies by Stampfli and Bennemann (1990, 1992) showed that the transverse-acoustic (TA)-phonon system becomes unstable if more than 8% of the valence electrons are excited to the conduction band. Atomic displacements were found to increase to around 1A˚ within 100–200 fs if 15% of the electrons are excited. On the basis of these results, the authors concluded that the resulting TA-phonon instability would lead to a rapid exchange of energy between the electrons and the atomic lattice in the form of mechanical work. A different approach was adopted by Silvestrelli et al. (1996), who performed *ab initio* molecular-dynamics calculations on the basis of finite-temperature density-functional theory to simulate ultrafast laser heating of silicon. Since the electron relaxation time (Agassi, 1984) is much

shorter than the electron–lattice relaxation time, the electron system remains in internal equilibrium at the initial laser-induced temperature and the ions are allowed to evolve freely. The simulation results showed that high concentrations of excited electrons can change the effective ion–ion interactions, thereby dramatically weakening the covalent bond and leading to a melting transition to a metallic state, which, in contrast to ordinary liquid silicon, is characterized by a high coordination number. The calculated ionic temperature after an elapsed time of about 100 fs was ~1700 K, i.e. close to the melting temperature of c-Si (Figure 2.13) defined as:

$$T_{\text{ion}}(t) = M / (3N-3)\, k_{\text{B}} \sum_{1=1}^{N} v^{2}{}_{1}(t), \qquad (2.7)$$

Where k_{B} is the Boltzmann constant, M is the Si ion mass, v_{i}(t) is the ionic velocity at time t, and N=64 is the number of atoms in the MD super cell representing the Brillouin zone. From Silvestrelli et al. (1996), reproduced with permission by the American Physical Society. These results are in sharp departure from the hypothesis that the phase transformation occurs with the lattice remaining relatively cold through a mechanical instability due to phonon softening.

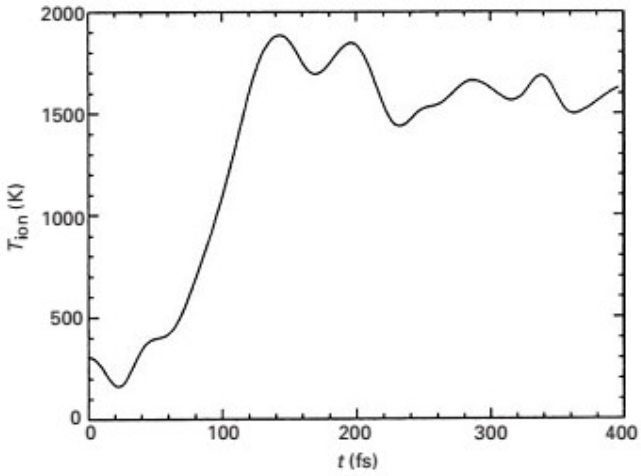

Figure 2.13: The time dependence of the instantaneous ionic temperature,

Femtosecond X-ray pulses have been used to study lattice dynamics (Rose-Petruck et al., 1999) and ultrafast melting (Chin et al., 1999; Larsson et al., 1998; Lindenberg et al., 2000, Siders et al., 1999; Cavalleriet al., 2000) associated with the fundamental phase-transition process. Visible probe light is absorbed within a short penetration depth and cannot accurately resolve nanometer-sized lattice distortion. Pulsed hard-X-ray sources are therefore advantageous for measuring atomic rearrangement and structural dynamics inside the target material. In addition to these observations, lattice disordering

was detected by depletion of diffracted X-ray images at the irradiation spot, indicating the occurrence of a nonthermal solid-to-liquid phase transition.

Figure 2.14 gives the schematic setup for the X-ray probe experiments (von der Linde et al., 2001). The 30-fs, 800-nm laser pulse output generated at 20 Hz by a Ti: Al_2O_3 laser was used for both sample excitation and X-ray generation. A split portion of these pulses was focused onto a moving Cu wire in vacuum, resulting in a point source of Cu Kα photons. The radiation emitted into two closely spaced lines, $K\alpha_1$and $K\alpha_2$, was diffracted by the sample that was excited by the optical pump pulse and detected by a sensitive X-ray CCD detector.

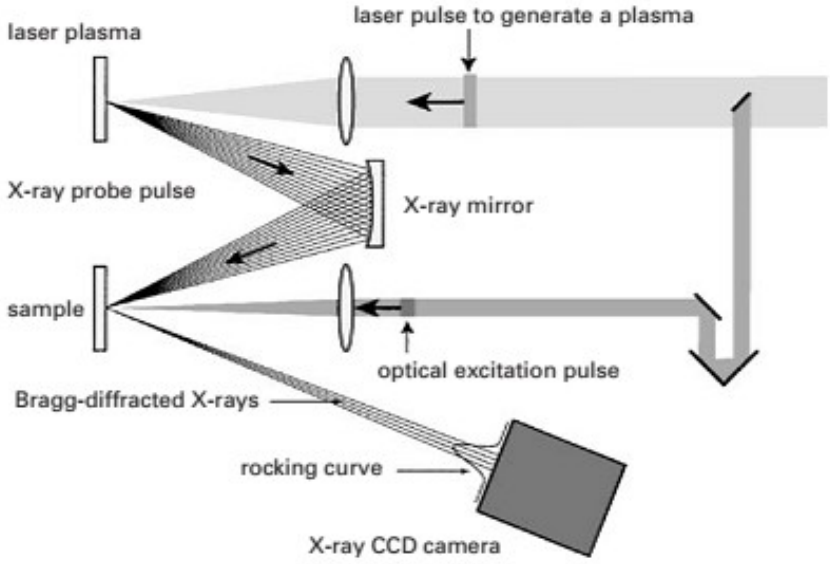

Figure2.14 The setup for the visible-pump, X-ray-probe experiments

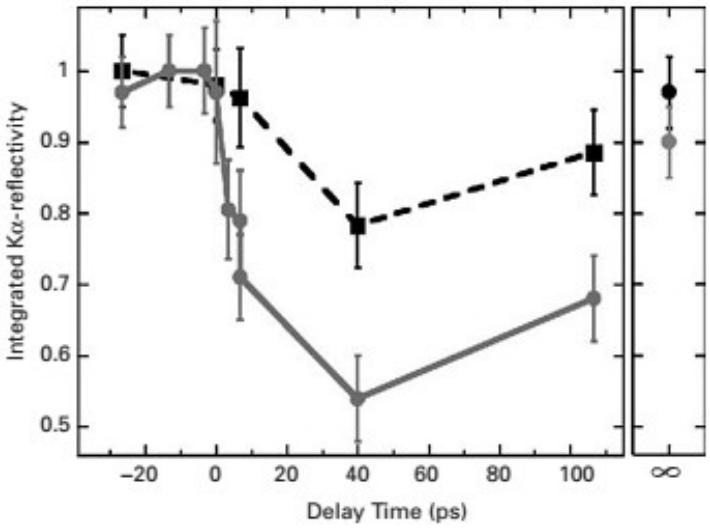

Figure 2.15 Time-resolved Kα X-ray reflectivity from a 160-nm Ge(111) film, integrated over the central pumped region (solid red line) and over a region vertically displaced by∼0.2 mm from the center (dashed black line). Measurement of non-thermal melting in germanium.

As shown in Figure 2.15, the diffraction signal dropped significantly within a few hundred femtoseconds in the region subjected to intensity sufficient for imparting homogeneous ultrafast melting. The significant drop in integrated diffracted intensity signified loss of crystalline order. At infinite time delays, the diffraction signal recovered to∼90% of the initial value (Siders et al., 1999), showing restoration of crystalline order, with the departure due either to amorphization or to ablative material loss. Since the integrated X-ray reflectivity scales with the material thickness, it was concluded that approximately 30–50 nm of the film undergoes ultrafast disordering. As argued previously, it has to be appreciated that the corresponding melting speed would have to be of the order of 10^4 m/s, which exceeds the speed of sound. In contrast, at near-threshold intensities the experiments show inhomogeneous melting evolving over a longer temporal scale that is consistent with a thermal phase-transition pathway.

2.4.1.2.2 Femtosecond-laser ablation of crystalline silicon:

Ultrashort pulsed laser processing of crystalline silicon has been studied experimentally (Choi and Grigoropoulos, 2002). The energy density provided by this laser beam focused to a 100-μm spot was sufficiently strong to ablate silicon. A pump-and-probe experiment was implemented, utilizing a time-delayed frequency-doubled (λ= 400 nm) beam for in situ reflectance measurements and observation by ultrafast microscopy. The deposition of the femtosecond-laser radiation generated a high-density electron–hole plasma that subsequently triggered ablation at about 10 ps (Figure 2.16).

Most of the ablated material was expelled on the nanosecond temporal scale. A shock wave was launched into the atmospheric-pressure air background. The position of this shock wave was monitored and analyzed by applying blast theory for an instantaneous point-source explosion.

Single shots at various laser fluences were used to fabricate micro-sized features as shown in Figure 2.17. Atomic-force microscopy (AFM) was used to measure detailed profiles of the modified features. In the lower-fluence regime, the density of hot electrons is relatively low and laser energy is mainly deposited in the shallow region defined by the optical penetration depth. Two-photon absorption and the electron-conduction term can be approximately taken into account by the introduction of an effective “laser+ electron heat” penetration depth. At higher fluences, the contribution of electron heat conduction becomes important, and the heat-affected region is defined by the electron heat penetration depth. The ablation efficiency

increased up to the fluence level around 10 J/cm^2, but, at higher fluences than 100 J/cm^2, it decreased significantly. In order to study the coupling mechanisms of the high-fluence femtosecond laser pulse with thetarget, time-resolved-pump-and-probe imaging data were presented as in Figure 2.18 for two fluence levels (10 and 1400 J/cm^2). Strong resistance during the expansion of the ablated plume leads to the generation of higher recoil pressure. This causes an increase in the redeposition and resolidification of the ablated materials, corresponding to a reduction of the ablation efficiency (Hwang et al., 2006), (Costas, 2009, pp. 158-168).

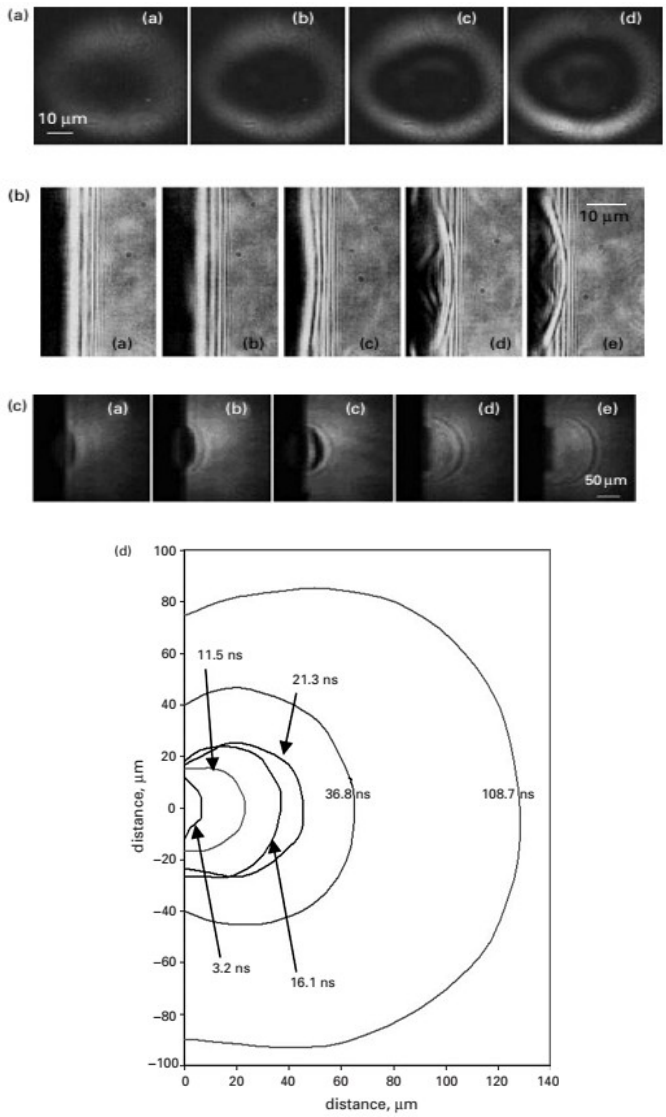

Figure 2.16: (a) Reflection images of a crystalline silicon surface subjected to femtosecond laser irradiation with *F*=1.5 J/cm^2. The darkening of the core region at 5–10 ps indicates initiation of the ablation process. (b) Shadowgraph images at early times. Material expulsion is visible at *t* =100 ps. (c) Shadowgraph images of the shock wave at long times. The ablation plume emerges from the surface. (d) The envelope of the shock wave at various elapsed times. The initial speed exceeds 1600 m/s.

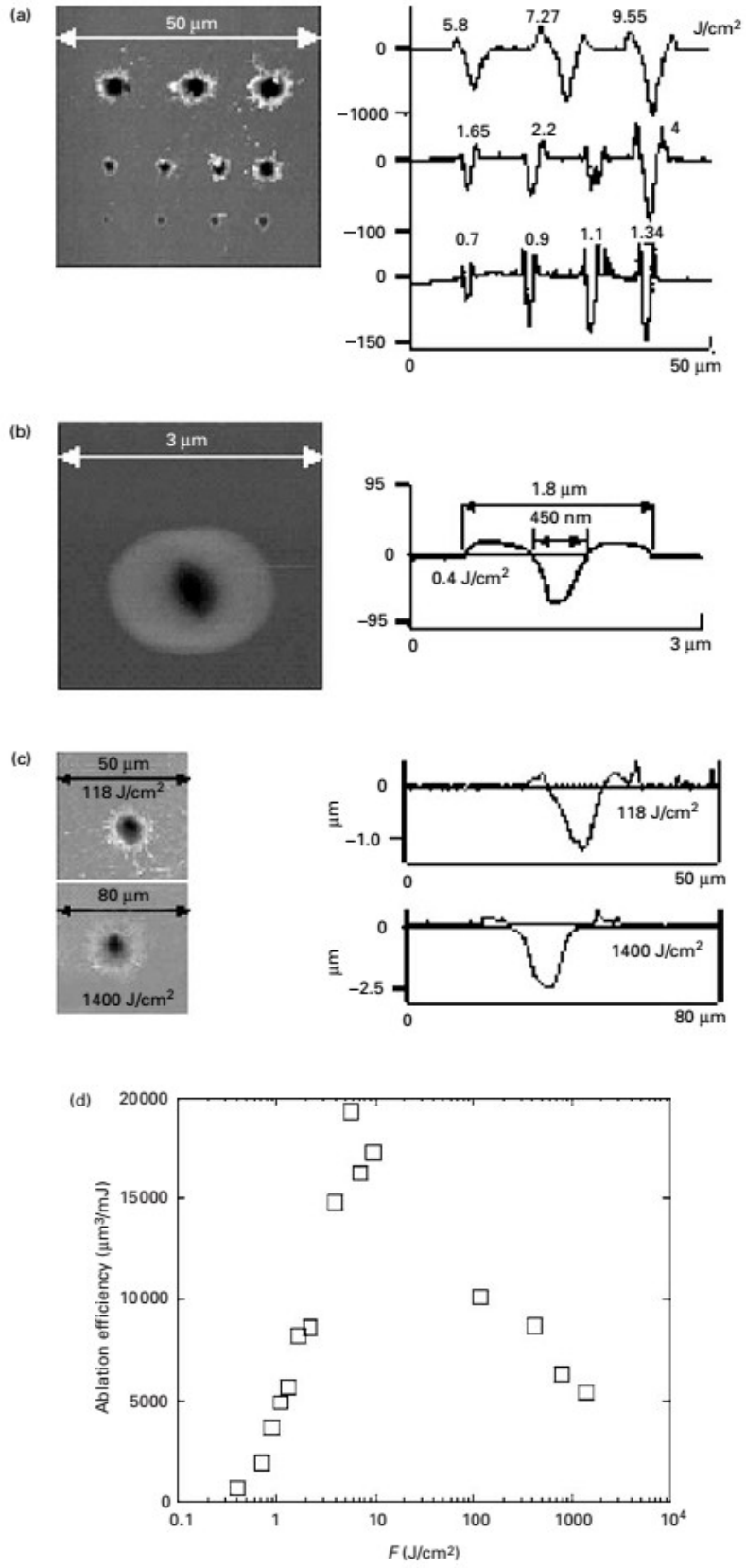

Figure 2.17: An AFM image and cross-sectional profile of a sub-micrometer hole being made to open in a c-Si wafer by single femtosecond laser pulses of λ=800 nm at medium energy densities (a), at near-threshold energy density (b), and at high energy densities (c); and the ablation efficiency as a function of the energy density (d). From Hwang et al.(2006), reproduced with permission by the American Institute of Physics.

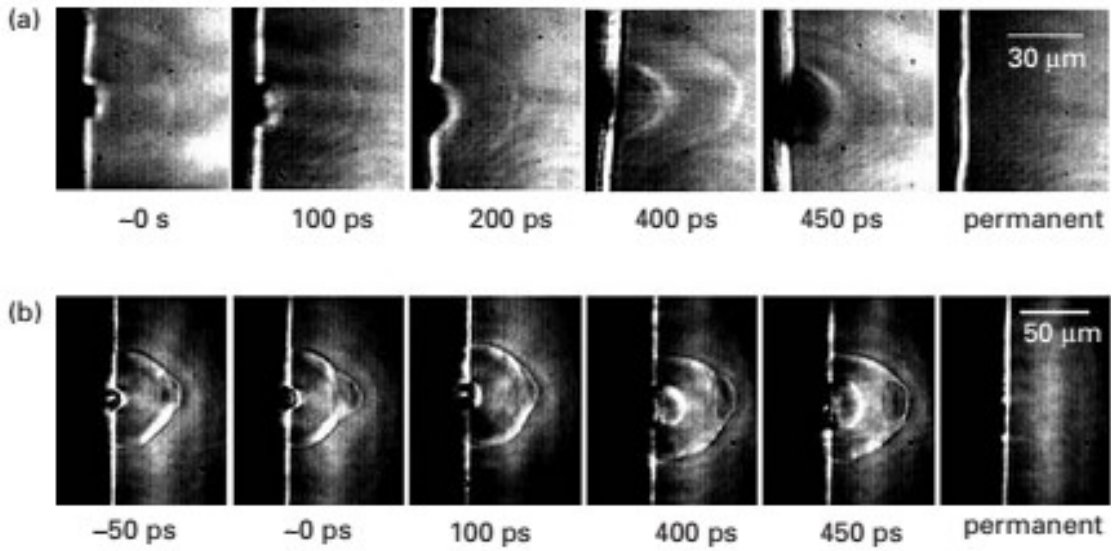

Figure 2.18 Time-resolved shadowgraphs (side view) of the silicon-ablation process: (a) F=11.2 J/cm^2 (285 nJ) (b); F=1400 J/cm^2(36.7µJ).

2.4.2 Laser-PMMA Interaction and Mechanical Stresses

2.4.2.1 Mechanisms of interaction and damage

The level on which a material modification is considered as damage depends on the material characteristics, laser wavelength, the energy and the shape of pulse, both temporal and spatial. The analysis of interaction is complete when all the phenomena occurring in the material are observed and the data of ejected material is recorded. The experiments with the control of both the ejected materials and the processes in the bulk are very complex.

Particular procedures are used to determine the damage threshold, which depends on the administrative regulations, on the purpose of the component application (medical, industrial) and is specific for each country.

2.4.2.2 Disintegration of polymers

Transparent and opaque (non-transparent) materials differ in effects of disintegration. Experimental data are useful in analyzing such effects in transparent amorphous and crystal materials. For simplest investigations, a Q-switch laser with regulated output power, lenses for beam focusing, a camera and investigated specimens are sufficient. Special care should be taken to aberrations of the optical system and elements, and particularly to new classes of aberrations connected to high-power laser systems. Two mechanisms are recognized: formation of rounded pores and formation of almost flat cracks (fissures). It seems that the type of disintegration in investigated power range depends only on the focal length of a lens; pores appear with greater focal length. The zone of disintegration has a conical form

with several dots as centers of scattering. Polystyrene and PMMA have similar behavior during the laser beam interaction. Of special interest is to observe the statistics of cracks formation. It is common to investigate the interaction with: low power (1-10 MW) and long focal length (50-{100 mm); high power (50-100 MW) and long focal length (50-100 mm); high power and short focal length (< 50 mm).

The influence of optical inhomogeneity and impurities to the threshold and character of disintegration is important. Both the kinetics of disintegration and the measurements of stress open new fields of investigation. Optical techniques for measurements, like photoelasticity, holography and optical tomography, were developed a long time ago. The potential role of newly developed ps and fs laser spectroscopies increases. The schematic of a polymer photodestruction is presented in Figure 2.19 and could be the object for analysis in photochemistries (Kovačević et al, 2007, p.982).

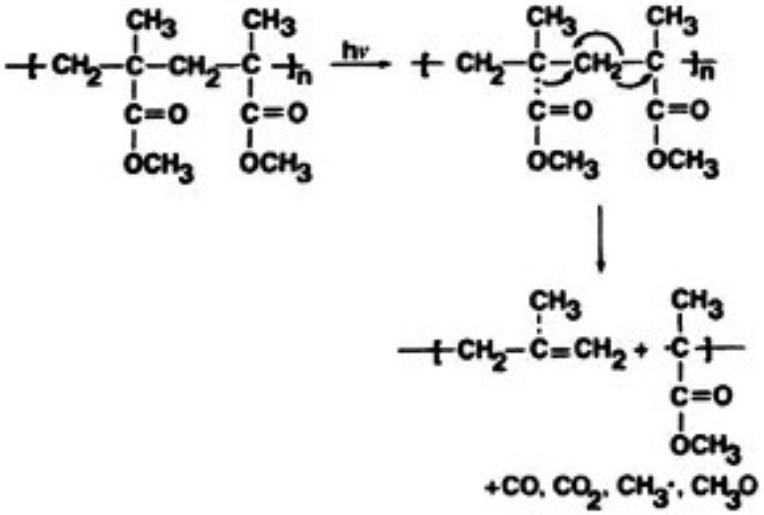

Figure 2.19: Some possible chain scissions of PMMA resist.

2.5 Raman Spectroscopy:

Raman spectroscopy is a spectroscopic technique based on inelastic scattering of monochromatic light, usually from a laser source. Inelastic scattering means that the frequency of photons in monochromatic light changes upon interaction with a sample. Photons of the laser light are absorbed by the sample and then reemitted. Frequency of the reemitted photons is shifted up or down in comparison with original monochromatic frequency, which is called the Raman effect. This shift provides information about vibrational, rotational and other low frequency transitions in molecules. Raman spectroscopy can be used to study solid, liquid and gaseous samples (Harris & Bertolucci, 1978).

2.5.1 Interaction of light with matter

Various processes can occur when light interacts with matter. In a case where the photon energy matches the deference between two real states of a molecule, the molecule can be excited into a higher electronic state. The excited molecule can relax to the ground state via a non-radiative process or via an additional luminous process (fluorescence). This process is used in absorption spectroscopy techniques such as infra-red (IR) spectroscopy. If the photon energy does not match the difference between the current state and another real state, it can be scattered inelastically (Brillouin and Raman scattering) or elastically (Rayleigh and Mie scattering). For an elastically scattered photon, the photon energy (wavelength) is the same before and after the scattering process. The process can be considered absorption of the photon (excitation of matter into a virtual intermediate state), which is followed by a prompt relaxation with re-emission of the photon. In contrast, inelastic Raman scattering is a nonlinear scattering process, involving quasiparticles such as phonons in a lattice or molecular vibrations (e.g., bending or rotation). The amount of energy change (either loss or gain) by a photon is characteristic for the nature of vibration (phonon or chemical bond). Nevertheless, not all vibrations will be observable with Raman spectroscopy because Raman scattering depends on symmetry and polarisability. Whereas IR-spectroscopy analyses the absorbed light of a broadband infra-red light source, Raman analyses inelastically scattered laser light randomly emitted in each direction (Harris & Bertolucci,1978).

2.5.2 Origins of Raman Effect

The Raman effect is based on molecular deformations in electric field E determined by molecular polarizability α. The laser beam can be considered as an oscillating electromagnetic wave with electrical vector E. Upon interaction with the sample it induces electric dipole moment $P = \alpha E$ which deforms molecules. Because of periodical deformation, molecules start vibrating with characteristic frequency υ_m.

Amplitude of vibration is called a nuclear displacement. In other words, monochromatic laser light with frequency υ_0 excites molecules and transforms them into oscillating dipoles. Such oscillating dipoles emit light of three different frequencies (Figure.2.20) when:

1. A molecule with no Raman-active modes absorbs a photon with the frequency υ_0. The excited molecule returns back to the same basic vibrational

state and emits light with the same frequency υ_0 as an excitation source. This type of interaction is called an elastic Rayleigh scattering.

2. A photon with frequency υ_0 is absorbed by Raman-active molecule which at the time of interaction is in the basic vibrational state. Part of the photon's energy is transferred to the Raman-active mode with frequency υ_m and the resulting frequency of scattered light is reduced to $\upsilon_0 - \upsilon_m$. This Raman frequency is called Stokes frequency, or just "Stokes".

3. A photon with frequency $\upsilon_0$is absorbed by a Raman-active molecule, which, at the time of interaction, is already in the excited vibrational state. Excessive energy of excited Raman active mode is released, molecule returns to the basic vibrational state and the resulting frequency of scattered light goes up to $\upsilon_0 + \upsilon_m$. This Raman frequency is called Anti-Stokes frequency, or just "Anti-Stokes".

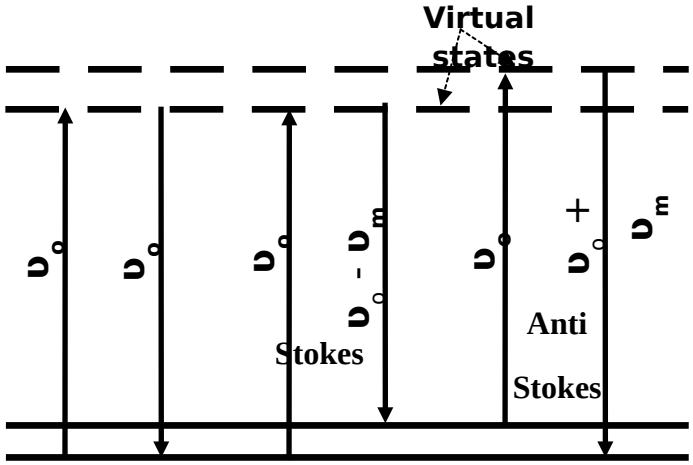

Figure 2.20: Raman transitional schemes

When the oscillating electric field of the excitation light is:

$$E = E_0 cos\,(\omega_{ex} t) \qquad (2.8)$$

And the induced dipole moment from this oscillating field is:

$$\mu_{induced} = \alpha E = \alpha E_0 cos\,(\omega_{ex} t) \qquad (2.9)$$

The molecular polarizability changes with bond length:

$$\alpha = \alpha_0 + (r - r_{eq}) d\alpha/dr \qquad (2.10)$$

The bond length oscillates at vibrational frequency is:

$$r - r_{eq} = r_{max} \cos(\omega_{vib} t) \quad (2.11)$$

Hence the polarizability oscillates at same frequency.

$$\alpha = \alpha_0 + [d\alpha/dr] r_{max} \cos(\omega_{vib} t) \quad (2.12)$$

Substitute.

$$\mu_{induced} = [\alpha_0 + [d\alpha/dr] r_{max} \cos(\omega_{vib} t)] E_0 \cos(\omega_{ex} t) = \alpha_0 E_0 \cos(\omega_{ex} t) +$$

$$E_0 r_{max} [d\alpha/dr] \cos(\omega_{ex} t) \cos(\omega_{vib} t) \quad (2.13)$$

Remember trig identity.

$$\cos x \cos y = 1/2[\cos(x + y) + \cos(x - y)] \quad (2.14)$$

$$\therefore \mu_{induced} = \alpha_0 E_0 \cos(\omega_{ex} t) + (E_0 r_{max})/2 [d\alpha/dr][\cos((\omega_{ex} + \omega_{vib}) t) +$$

$$\cos((\omega_{ex} - \omega_{vib}) t)] \quad (2.15)$$

Induced dipole has Rayleigh, Stokes, and anti-Stokes components.

About 99.999% of all incident photons in spontaneous Raman undergo elastic Rayleigh scattering. This type of signal is useless for practical purposes of molecular characterization. Only about 0.001% of the incident light produces inelastic Raman signal with frequencies $\upsilon_0 \pm \upsilon_m$. Spontaneous Raman scattering is very weak and special measures should be taken to distinguish it from the predominant Rayleigh scattering. Instruments such as notch filters, tunable filters, laser stop apertures, double and triple spectrometric systems are used to reduce Rayleigh scattering and obtain high-quality Raman spectra.

2.5.3 Raman Selection Rules and Intensities

A simple classical electromagnetic field description of Raman spectroscopy can be used to explain many of the important features of Raman

band intensities. The dipole moment, P, induced in a molecule by an external electric field, E, is proportional to the field

$$P = \alpha E \qquad (2.16)$$

The proportionality constant α is the polarizability of the molecule. The polarizability measures the ease with which the electron cloud around a molecule can be distorted. The induced dipole emits or scatters light at the optical frequency of the incident light wave. Raman scattering occurs because a molecular vibration can change the polarizability. The change is described by the polarizability derivative, $d\alpha/dQ$, where Q is the normal coordinate of the vibration. The selection rule for a Raman-active vibration, that there be a change in polarizability during the vibration, is

$$d\alpha/dQ \neq 0 \qquad (2.17)$$

Selection rules related to symmetry:

Rule of thumb: symmetric = Raman active, asymmetric = IR active.

The Raman selection rule is analogous to the more familiar selection rule for an infrared-active vibration, which states that there must be a net change in permanent dipole moment during the vibration. From group theory it is straightforward to show that if a molecule has a center of symmetry, vibrations that are Raman active will be silent in the infrared, and vice versa. Scattering intensity is proportional to the square of the induced dipole moment, i.e., to the square of the polarizability derivative.

If a vibration does not greatly change the polarizability, then the polarizability derivative will be near zero, and the intensity of the Raman band will be low. The vibrations of a highly polar moiety, such as the O-H bond, are usually weak. An external electric field cannot induce a large change in the dipole moment and stretching or bending the bond does not change this. In organic molecules, particularly, certain frequencies can be associated with typical types of molecular excitations such as C ≡ C triple bond stretching (Harris & Bertolucci,1978).

2.5.4 Raman Spectrum

A complete Raman spectrum consists of a Rayleigh scattered peak (high intensity, same wavelength as excitation), a series of Stokes-shifted peaks (low intensity, longer wavelength), a series of anti-Stokes shifted peaks (still lower intensity, shorter wavelength) and the spectrum independent of excitation wavelength (488, 632.8, or 1064 nm) (Luppnow et al, 2003).

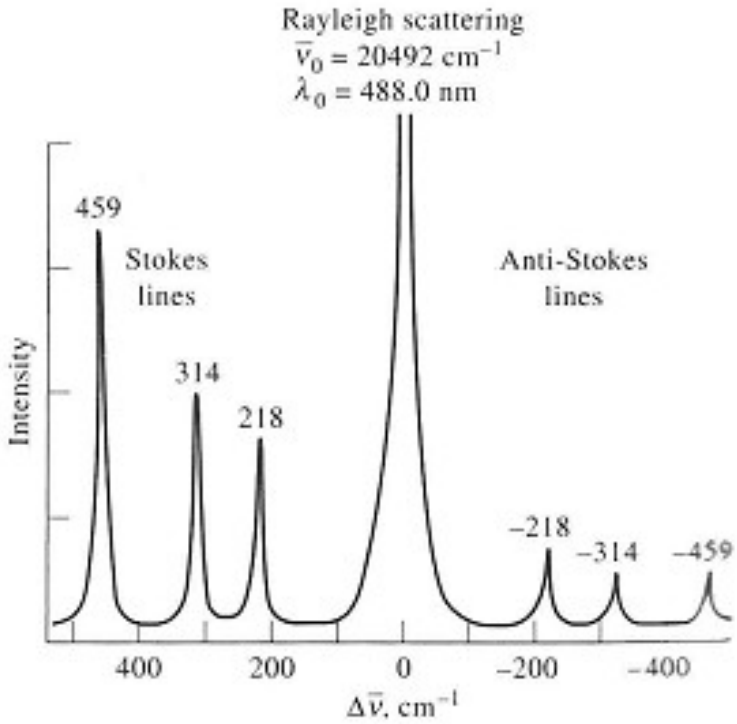

Figure2.21: Spectrum of CCl_4, using an Ar^+ laser at 488 nm.

2.5.5 Information from Raman Spectroscopy

Characteristic Raman frequencies gives composition of material e.g. MoS_2, MoO_3 , changes in frequency of Raman peak gives stress/strain state e.g. Si 10 cm^{-1} shift per % strain, polarization of Raman peak gives crystal symmetry and orientation e.g. orientation of CVD diamond grains, width of Raman peak gives quality of crystal e.g. amount of plastic deformation and intensity of Raman peak gives amount of material e.g. thickness of transparent coating .

2.5.6 Instrumentation

A Raman system typically consists of four major components:

1. Excitation source (Laser).

2. Sample illumination system and light collection optics.

3. Wavelength selector (Filter or Spectrophotometer).

4. Detector (Photodiode array, CCD or PMT).

A sample is normally illuminated with a laser beam in the ultraviolet (UV), visible (Vis) or near infrared (NIR) range. Scattered light is collected with a

lens and is sent through interference filter or spectrophotometer to obtain Raman spectrum of a sample.

Since spontaneous Raman scattering is very weak the main difficulty of Raman spectroscopy is separating it from the intense Rayleigh scattering. More precisely, the major problem here is not the Rayleigh scattering itself, but the fact that the intensity of stray light from the Rayleigh scattering may greatly exceed the intensity of the useful Raman signal in the close proximity to the laser wavelength. In many cases the problem is resolved by simply cutting off the spectral range close to the laser line where the stray light has the most prominent effect. People use commercially available interference (notch) filters which cut-off spectral range of ± 80-120 cm^{-1} from the laser line. This method is efficient in stray light elimination but it does not allow detection of low-frequency Raman modes in the range below 100 cm^{-1}.

Stray light is generated in the spectrometer mainly upon light dispersion on gratings and strongly depends on grating quality. Raman spectrometers typically use holographic gratings which normally have much less manufacturing defects in their structure then the ruled once. Stray light produced by holographic gratings is about an order of magnitude less intense then from ruled gratings of the same groove density.

Using multiple dispersion stages is another way of stray light reduction. Double and triple spectrometers allow taking Raman spectra without use of notch filters. In such systems Raman-active modes with frequencies as low as 3-5 cm^{-1} can be efficiently detected.

In earlier times people primarily used single-point detectors such as photon-counting Photomultiplier Tubes (PMT). However, a single Raman spectrum obtained with a PMT detector in wavenumber scanning mode was taking substantial period of time, slowing down any research or industrial activity based on Raman analytical technique. Nowadays, more and more often researchers use multi-channel detectors like Photodiode Arrays (PDA) or, more commonly, a Charge-Coupled Devices (CCD) to detect the Raman scattered light. Sensitivity and performance of modern CCD detectors are rapidly improving. In many cases CCD is becoming the detector of choice for Raman spectroscopy.

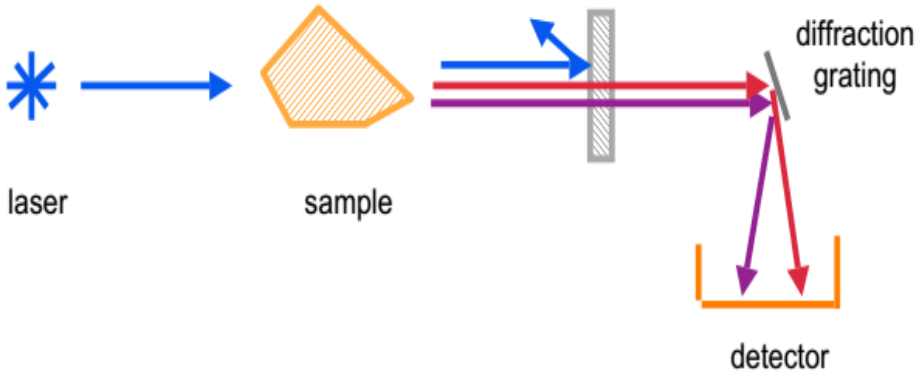

Figure 2.22: Generic Raman system flow diagram

Figure 2.22 shows generic Raman system flow diagram, illuminate a Sample with an intense single frequency light source and measure the relative frequency shift of the inelastically scattered light. Simplified Raman spectrometer layout is shown below in Figure 2.23.

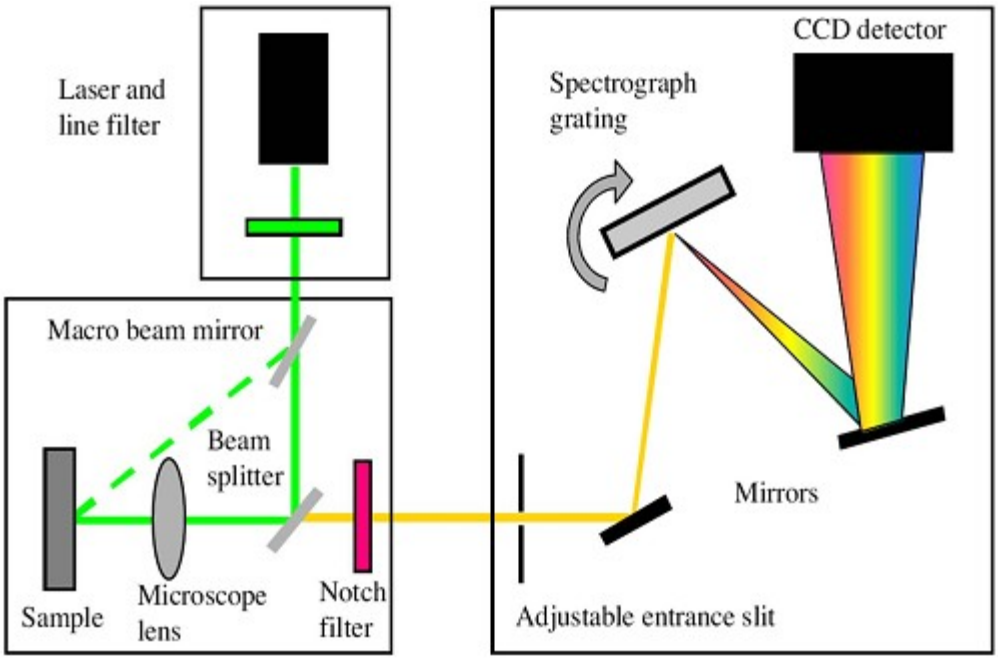

Figure 2.23: Simplified Raman spectrometer layout

2.5.7 Laser wavelength selection concerns for classical Raman

As the laser wavelength gets shorter Raman scattering efficiency increases, the risk of fluorescence increases (except deep UV), the risk of sample damage / heating increases and the cost of the spectrometer increases. Want to use short wavelength because scattering depends on 4th power of frequency but want to use long wavelength to minimize chance of inducing fluorescence see figure 2.24.

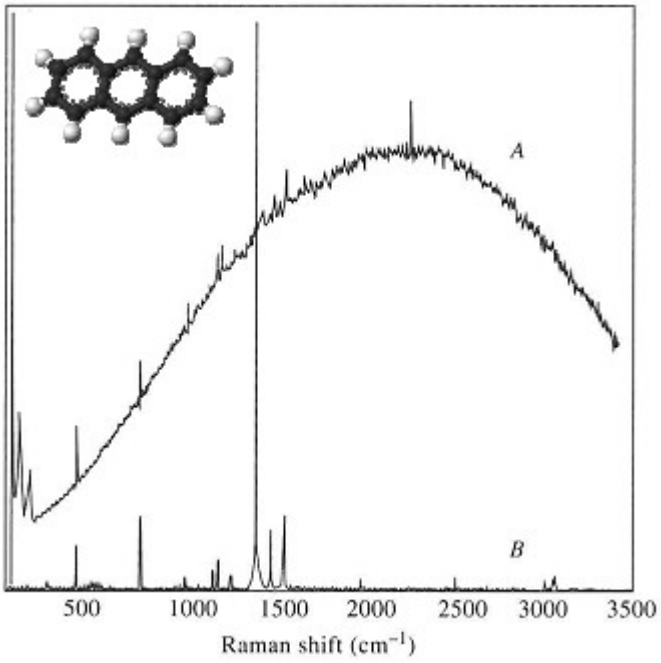

Figure 2.24: Spectrum of anthracene. A: using Ar^+ laser at 514.5 nm. B: using Nd:YAG laser at 1064 nm.

2.5.8 Raman light sources

Raman intensity is weak and the excitation source must be strong to generate sufficient signal. Source must be monochromatic so that spectrum is sufficiently uncomplicated. Intense lamps can work, but when monochromatized, have very little power. Scattering efficiency increases as ν^4: the bluer the light, the more the scattering.2The bluer the light, the greater the chance of producing fluorescence. Lasers are used almost exclusively: Ar^+Ion: 488.0 and 514.5 nm, Kr^+ Ion: 530.9 and 647.1 nm, He:Ne: 632.8 nm, Diode Lasers: 782 and 830 nm and Nd: YAG: 1064 (532 when doubled) nm. Examples of lasers and its purposes:

1) UV lasers Common excitation wavelengths

244 nm- biological, catalysts (Resonance Raman)

325 nm- wide band-gap semiconductors

2) Visible lasers

488 nm & 514 nm- semiconductor, catalysts, biological, polymers, minerals & general purpose

633 nm- corrosion & general purpose

3) NIR lasers

785 nm - polymers, biological & general purpose

830 nm- biological

2.5.9 Methods to improve Raman signal intensity

Raman signal is normally quite weak and people are constantly improving Raman spectroscopy techniques. Many different ways of sample preparation, sample illumination or scattered light detection were invented to enhance intensity of Raman signal. Here we will examine some of them.

2.5.9.1 Stimulated Raman Spectroscopy

It was found that if the sample was irradiated with a very strong laser pulse, new “non-linear” phenomena were observed in Raman signal. In comparison with continuous wave (CW) lasers with electric field of about only 10^4 V·cm^{-1} pulsed lasers with electric field of about 10^9 V·cm^{-1} transform a much larger portion of incident light into useful Raman scattering and substantially improve signal-to-noise ratio.

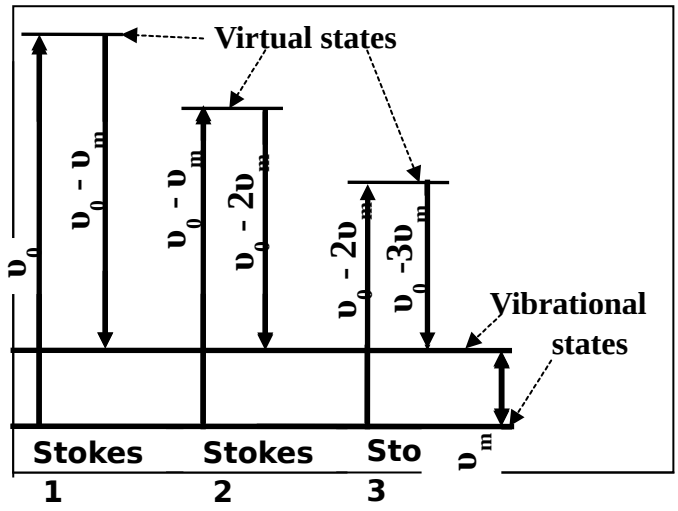

Figure 2. 25: Stimulated Raman transitional schemes

Stimulated Raman scattering is an example of “non-linear” Raman spectroscopy. Very strong laser pulse with electric field strength > 10^9 V·cm^{-1} transforms up to 50% of all laser pulse energy into coherent beam at Stokes frequency $\upsilon_0 - \upsilon_m$ (Figure. 2.25).The Stokes beam is unidirectional with the incident laser beam. Only the mode um which is the strongest in the regular Raman spectrum is greatly amplified. All other, weaker Raman active modes are not present. The Stokes frequency is so strong it acts as a secondary excitation source and generates the second Stokes line with frequency $\upsilon_0 - 2\upsilon_m$. The second Stokes line generates the third one with the frequency $\upsilon_0 - 3\upsilon_m$ etc.

Stimulated Raman technique enjoys 4-5 orders of magnitude enhancement of Raman signal as compared to the spontaneous Raman scattering.

2.5.9.2 Coherent Anti-Stokes Raman Spectroscopy (CARS)

Coherent Anti-Stokes Raman, CARS, is another type of “non-linear” Raman spectroscopy. It stands for Coherent Anti-Stokes Raman Spectroscopy. Instead of the traditional one laser, two very strong collinear lasers irradiate a sample. Frequency of the first laser is usually constant, while the frequency of the second one can be tuned in a way that the frequency difference between the two lasers equals exactly the frequency of some Raman-active mode of interest. This particular mode will be the only extremely strong mode in the Raman signal. With CARS we can obtain only one strong Raman peak of interest. In this case a monochromator is not really required. A wideband interference filter and a detector behind the filter would do the job. Below is more specific description with a little bit of math to understand CARS more in depth.

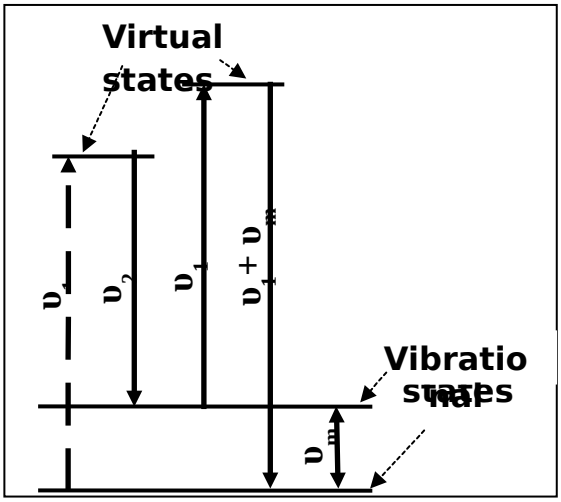

Figure 2.26: Transitional scheme for CARS

Two laser beams with frequencies $\upsilon_1$and υ_2(υ_1> υ_2) interact coherently, and because of the wave mixing, produce strong scattered light of frequency $2\upsilon_1$- υ_2 (Figure 2.26). If the frequency difference between two lasers υ_1- $\upsilon_2$is equal to the frequency um of a Raman-active rotational, vibrational or any other mode then a strong light of frequency $\upsilon_1 + \upsilon_m$is emitted.

In other words, to obtain strong Raman signal the second laser frequency should be tuned in a way that $\upsilon_2 = \upsilon_1 - \upsilon_m$. Then the frequency of strong scattered light will be $2\upsilon_1 - \upsilon_2 = 2\upsilon_1 - (\upsilon_1 - \upsilon_m) = \upsilon_1 + \upsilon_m$, which is higher than the excitation frequency υ_1 and therefore considered to be Anti-Stokes frequency.

Coherent Anti-Stokes Raman Spectroscopy derives its name from the fact that it uses two Coherent laser beams and the resulting signal has Anti-Stokes frequency.

2.5.9.3 Resonance Raman Spectroscopy (RR)

Many substances, especially colored ones, may absorb laser beam energy and generate strong fluorescence which contaminates Raman spectrum. This is one of the central problems in Raman spectroscopy especially when UV lasers are used.

However, it was found that under certain conditions some types of colored molecules can produce strong Raman scattering instead of fluorescence. This effect was called Resonance Raman. The Resonance Raman effect takes place when the excitation laser frequency is chosen in a way that it crosses frequencies of electronic excited states and resonates with them. Intensity of Raman bands which originate from electronic transitions between those states are enhanced 3-5 orders of magnitude. Not all the bands of spontaneous Raman spectrum are enhanced. The so-called chromophoric group, which is responsible for the molecule's coloration, experiences the highest level of enhancement. The reason is the chromophoric group normally has the highest level of light absorption.

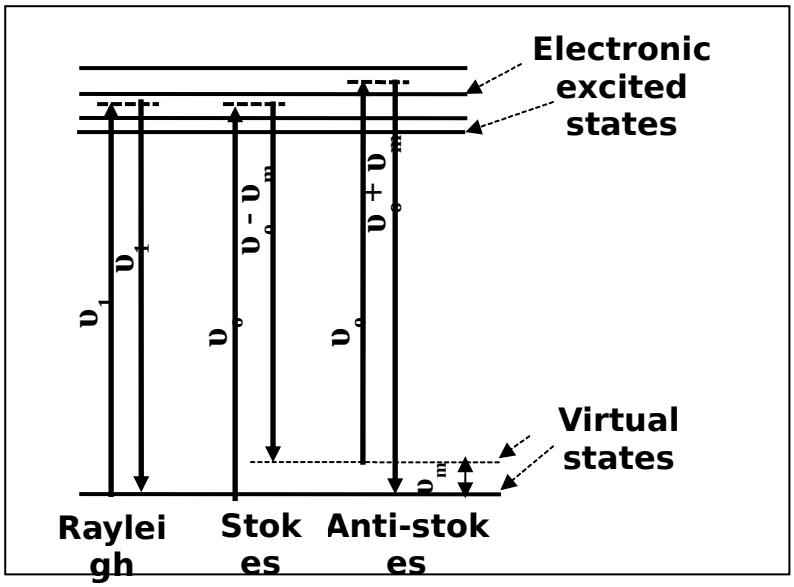

Figure 2.27: Resonance Raman transitional schemes

The highest intensity of Resonance Raman signal is obtained when laser frequency equals to the first or the second electronic excited state (Figure 2.27). Therefore, tunable lasers are the most appropriate choice for the RR technique. Although , even when the frequency of the laser does not

exactly match the desired electronic excited states an impressive enhancement of Raman signal occurs.

2.5.9.4 Surface-Enhanced Raman Spectroscopy (SERS) and Surface-Enhanced Raman Resonance Spectroscopy SERRS

Surface-Enhanced Raman Spectroscopy utilizes the following effect. Raman signal from molecules adsorbed on certain metal surfaces can be 5-6 orders of magnitude stronger then the Raman signal from the same molecules in bulk volume. The exact reason for such dramatic improvement is still under discussion. However, since intensity of Raman signal is proportional to the square of electric dipole moment $P = \alpha E$, there are two possible reasons - the enhancement of polarizability α, and the enhancement of electrical field E.

The first enhancement of polarizability a may occur because of a charge-transfer effect or chemical bond formation between metal surface and molecules under observation. This is a so-called chemical enhancement.

The second one takes into account interaction of the laser beam with irregularities on the metal surface such as metal micro-particles or roughness profile. It is believed that laser light excites conduction electrons at the metal surface leading to a surface plasma resonance and strong enhancement of electric field E. It is also called electromagnetic enhancement.

In all cases choice of appropriate surface substrate is very important. The most popular and universal substrates used for SERS are electrochemically etched silver electrodes as well as silver and gold colloids with average particle size below 20 nm.

One disadvantage of SERS is the difficulty of spectra interpretation. The signal enhancement is so dramatic that Raman bands that are very weak and unnoticeable in spontaneous Raman spectra can appear in SERS. Some trace contaminants can also contribute additional peaks. On the other hand, because of chemical interactions with the metal surface, certain peaks which are strong in conventional Raman might not be present in SERS at all. Non-linear character of signal intensity as a function of concentration complicates things even further. Very careful consideration of all physical and chemical factors should be done while interpreting SERS spectra which makes it extremely difficult for practical use.

The SERRS technique, Surface-Enhanced Resonance Spectroscopy, was developed because of such complications. It utilizes both Surface-Enhancement effect and Raman Resonance effect so the resulting

enhancement in Raman signal intensity can be as high as 10^{14}. The main advantage of SERRS is its spectra resemble very much regular Resonance Raman spectra, which makes it much easier to interpret (Piacton,2014).

2.5.10 Raman Spectroscopy Advantages

Here are some reasons why someone would prefer to use Raman Spectroscopy.

• Non-destructive to samples (minimal sample prep)

• Higher temperature studies possible (don't care about IR radiation)

• Easily examine low wavenumber region: 100 cm^{-1} readily achieved.

• Better microscopy; using visible light so can focus more tightly.

• Easy sample prep: water is an excellent solvent for Raman. Can probe sample through transparent containers (glass or plastic bag) (Luppnow et al, 2003).

2.5.11 Applications of Raman mapping

The fast mapping Raman instrument is ideal for the study of any material having spatially varying chemical composition. Typical applications include:

1. **Pharmaceutical products**

   Mapping the distribution of active ingredients and excipients

   Characterization of controlled-release systems

   Stability studies

2. **Filled or composite materials**

   Non-destructive depth profiling

   Real time dynamic cure studies of resins and adhesives

3. **Analysis of defects and contamination Material Morphology**

   Polymorph distributions

   Crystallinity and orientation studies

4. **Medical Devices**

   Compositional analysis of complex structures including stents and catheters

   QA and failure analysis (Intertek, 2014).

Chapter Three

Experimental part

In this chapter the method to produce surface gratings on PMMA and Si based on LDW technique and characterization of the produced surface are presented.

3.1 Fabricating surface gratings setup

To demonstrate the Laser Direct Writing technique, we adopt two different laser systems which we used to produce surface gratings in PMMA and Si.

3.1.1 The Materials

PMMA samples with a thickness of ~1 mm, and an area of 2cm × 2cm were used in the experiments. The sides were polished using alumina powder and polishing sheets of different fine grades. The writing system is schematically shown in Figure 3.1.

Silicon samples had the following parameters: thickness ~330 μm, resistivity 1Ω.cm and area 2cm × 2cm. Silicon samples were selected to surface texture treatment and to measure its effect on the spectral responsivity. The writing system is schematically shown in Figure 3.4.

3.1.2 The irradiation setup

This part of experimental portion of this work deals with the setup of laser treatments to irradiation processes of the samples in one dimension for PMMA samples and one dimension and two dimension for silicon samples. Two types of setups were utilized, the first one used a fibre beam delivery system for the PMMA samples and the second one was an articulated beam delivery system for silicon samples.

3.1.2.1 PMMA

The writing system is schematically shown in Figure 3.1 (a and b). This setup is composed of:

(1) Laser source: ora-laser jet 20 (The ora-laser jet is 810 nm diode laser with up to 20 Watts power at the fibre tip, microprocessor controlled power output) Figure 3.2. The PMMA sample was irradiated by a CW diode laser with 0.3 Watt power at 810 nm wavelength of operation.

(2) Beam delivery system: This system is composed of the fibre tip of the laser source and a holder.

(3) Substrate or target mounting system.

(a

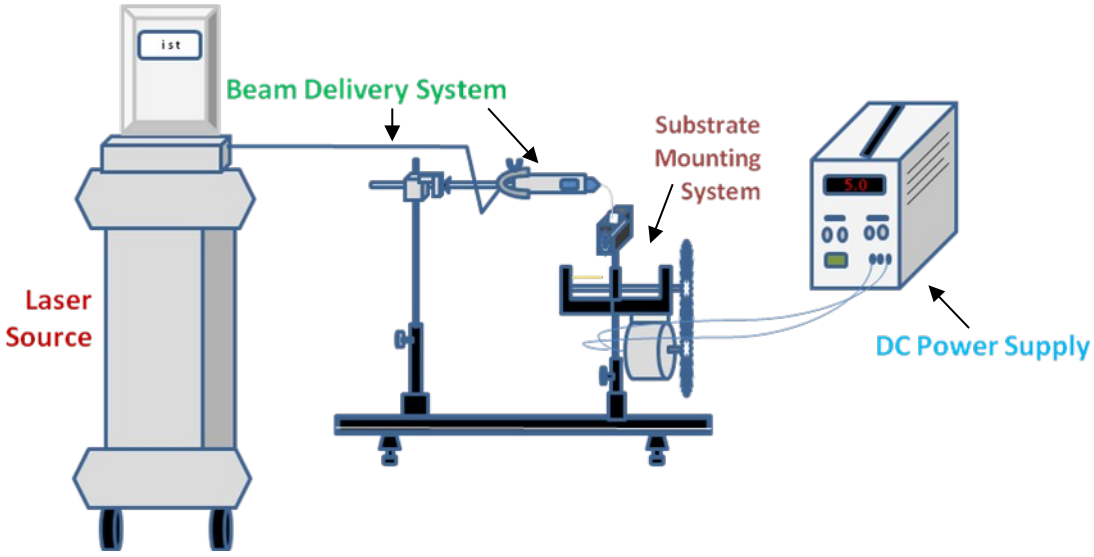

(b

Figure 3.1Experimental setup used in this study. A) Photograph b) Schematic diagram.

Three dimensions moving table is a home-built made using available tools and equipments at the lab to mounting the sample. The movable table moves linearly by a DC linear motor .The platform could

be translated the sample along the x-direction so that the laser beam scribed parallel structures, line by line along x-axis to produce the desired structure. The speed was determined by adjusting specific voltages of the motor. The speed of irradiation was about 4 mm/s. The specimen vertically shifted with screw in steps of about 50 µm.

Figure 3.2 ora-laser jet 20

3.1.2.2 Silicon

The writing system is schematically shown in Figure 3.3. This setup is composed of:

(1) laser source:

The Si sample was irradiated by means of Coherent Legend Ti: sapphire laser facility generated horizontal linear polarized light, pulsed at a

1- kHz repetition rate, with pulse duration of 130-fs at a central wavelength of 800nm. The output beam from the system had a laser power of ~3 W in the Gaussian mode with a diameter of ~7 mm.

(2) Beam delivery system: (articulated)

The laser beam was attenuated by a diffractive optic attenuator and its frequency was doubled by a BBO crystal, generating fs laser irradiation at 400 nm wavelength. A small integrated fluence is created by natural density

(ND) filter placed between the reflection mirrors. The laser beam passed through two UV mirrors to reduce the residuals IR radiation. The laser beam was focused to ~8 µm diameter by a 20 X Nikon microscope objective with a0.45 numerical aperture (NA), 10 mm focal length and long working distance of 8 mm.

(3) Substrate or target mounting system.

The sample under study is mounted on a PC controlled Aerotech x-y-z translation stage (ANT-25LV) of 2.5 nm resolution and the fabrication process was viewed by CCD Camera. The experiments were performed by translating the sample along the x-direction so that the laser beam scribed parallel structures, line by line along x-axis.

The experiments using Si samples involved two main steps of investigation: (1) the influence of laser power variation while the irradiation spacing is constant into the sample, (2) the structural dimension created at different spacing with the fixed pulse energy while the translation speed is constant in all irradiation processes.

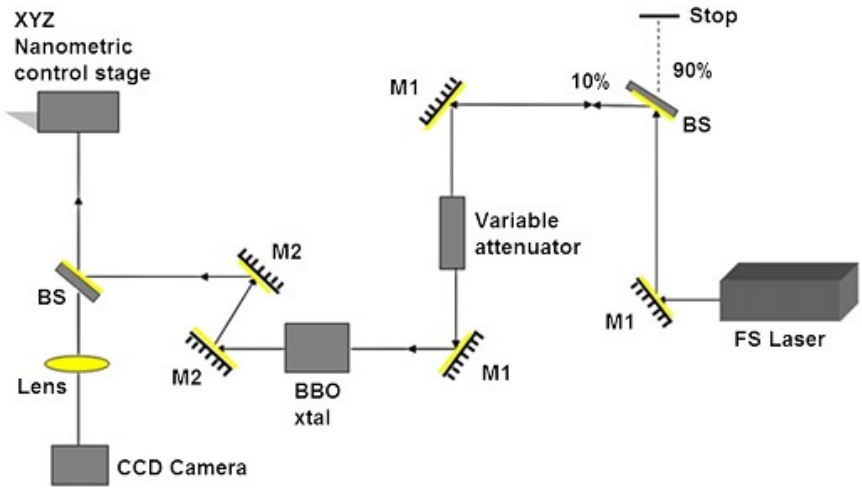

Figure3.3 The experimental setup of surface irradiation technique, $M_1$50 mm diameter IR mirrors, and $M_2$50 mm diameter UV mirrors.

3.2 Characterizing the produced surface changes

This part of experimental work deals with characterizations of the written surfaces.

3.2.1 Scanning electron microscopy (SEM)

A JCM-6000 NeoScope Benchtop SEM (Figure 3.4) scanning electron microscope was used to characterize surface texture in irradiated regions and non irradiated regions. A scanning Electron Microscope (SEM) images of the

structures obtained in air environment. The beam conditions were 15 KeV acceleration with a 1 nA beam current.

Figure 3.4 JCM-6000 NeoScope Benchtop SEM

3.2.2 Raman mapping

Raman scattering measurements have been carried out using SENTERRA Raman spectrophotometer shown in figure 3.5 to obtain the Raman spectrum of various samples in irradiated points and other non-irradiated. This spectrometer utilizes a 532 nm, laser to excite the molecular vibrations, spectral range was from 500-1800 cm^{-1}.

Figure3.5 SENTERRA Raman spectrophotometer

3.2.3 Diffraction patterns achievement

The diffraction pattern, from the written surface gratings, was achieved through illuminating PMMA grating with a 1 mW He–Ne laser (632.8 nm)and Si grating with a He–Ne laser (632.8 nm) and Argon-ion laser (514.5 nm).

3.2.4 Silicon photovoltaic's Spectral Response Measurement

The spectral response of the samples is measured by standard method using computerized monochromatic before and after the irradiation process. The system instrumentation is controlled by a PC via the RS232 interface. The output of the monochromator is directed to two output windows. One beam is directed to a calibrated detector and the other to the sample under test. During the system operation a broad band light source is passed through a monochromator signaling the desired frequency of the light illuminating the photodiode. The photovoltaic device current is measured by means of the semiconductor parameter analyzer and the results are stored on the PC. The measurements are then repeated in the (400-900) nm wavelength range.

The results of the experimental work will be summarized and presented in chapter four.

Chapter Four

Results and Discussion

The purpose of this chapter is to present and discuss the results of the experimental work on interaction of the laser beam with PMMA and silicon samples.

4.1Scanning electron microscopy SEM of the Irradiated samples:

4.1.1: PMMA scanning electron microscopy:

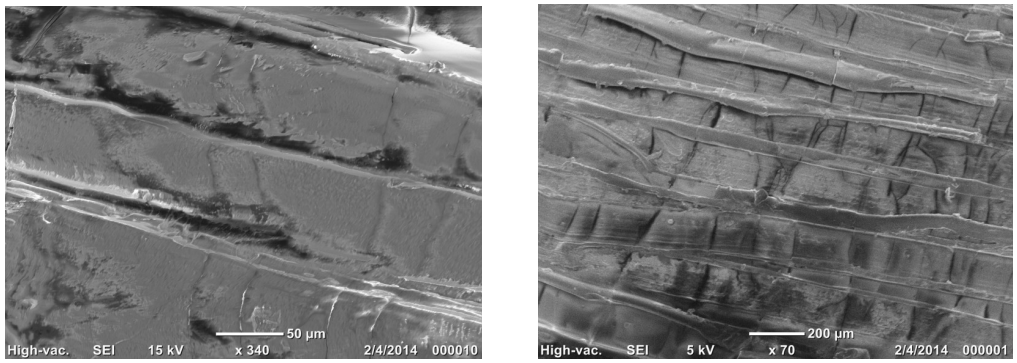

a) One groove (Scale bar is 50 µm) **b) Multi-grooves (Scale bar is 200 µm)**

c) Multi-grooves (Scale bar is 300 µm) **d) Multi-grooves (Scale bar is 500µm)**

Figure 4.1 SEM images for one dimensional PMMA irradiated samples; the operating microscope voltage is 5 kV

Figure 4.1 shows the SEM images of surface structure after IR laser irradiation, it is obvious from the images that surface textures have been formed upon laser treatment. The textured PMMA surface is observed at different magnifications as 300X & 150X, figure 4.1 (c) & (d) respectively. Images show also laser-ablated and laser-melted PMMA surfaces. Estimated grooves spacing of the gratings of various microns have been written on the surface of the PMMA slabs.

4.1.2: Silicon scanning electron microscopy:

A semi periodic structure is formed and observed in the range of (700-900) nm for one groove. The SEM images show a semi periodic structure known as ripples or grooves in the sub-micrometer range, as shown in figure 4.2 and figure 4.3.

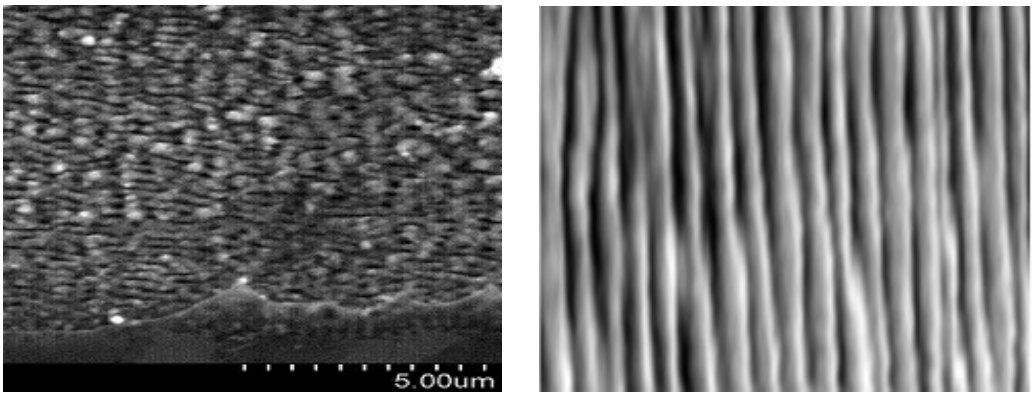

a) Scale bar is 5µm. **b) 12µm width.**

Figure 4.2 a) one groove, b) the periodic structured, of the one dimensional irradiated cell, by a100fs laser pulses, 387nm wavelength.

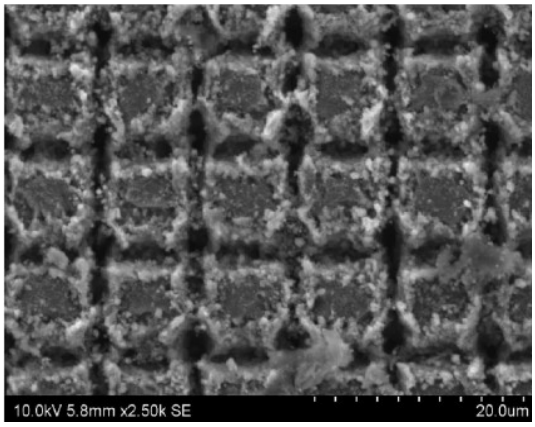

Figure 4.3 SEM image for two dimensional irradiated sample, Scale bar is 20 µm. The operating microscope voltage is 10kV

4.2 Raman mapping of PMMA Irradiated samples:

The main goal of this spectroscopic characterization was to investigate the photothermal and photochemical modifications, of the irradiated material, that induced by the CW diode laser. Since the PMMA is well known to undergo the process of chain scission and cross-linking when exposed to the radiation of various wavelengths, figure 4.4 shows schematically these key processes taking place inside the irradiated PMMA. It is obvious the effect of chain scission is essentially responsible for the producing of tiny volatile fragments, such as methyl or ester groups, etc., which easily escape the material surface. On the other hand, when free end-links are present in the irradiated material, the effect of cross-linking can take place. This effect is indicated by means of a formation of double

C=C bonds in the backbone chain of the PMMA which originally contains only single C–C bonds.

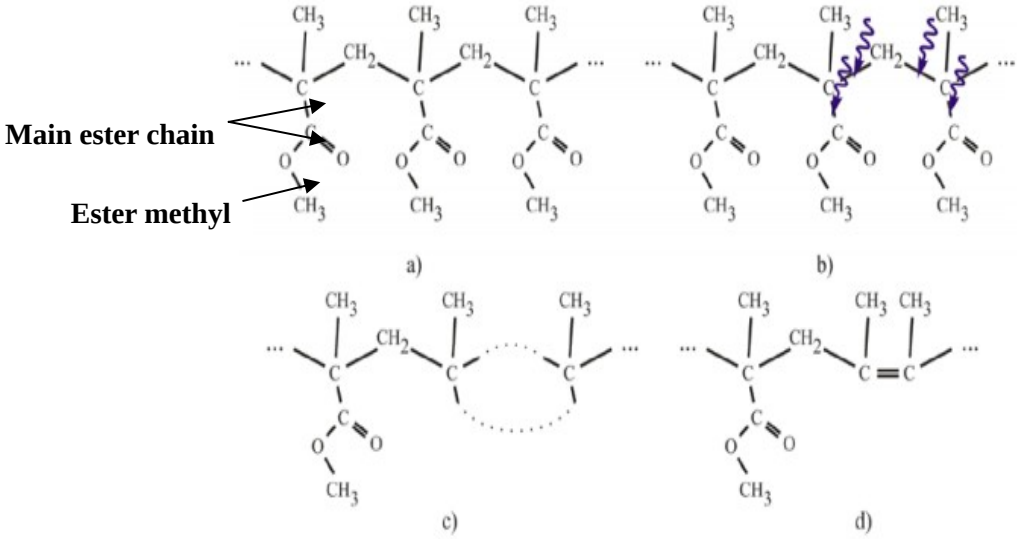

Figure 4.4 Formation of a PMMA molecule with a double bond C=C; (a) unaffected PMMA molecule, (b) chain scission caused by incident radiation, (c) and (d) cross-linking.

Figure 4.5 (a, b and c) below show the Points where Raman spectra were collected from different regions in the fabricated structures at 10 mW powers, point one: un-irradiated area, point two: melting area, point three: ablation

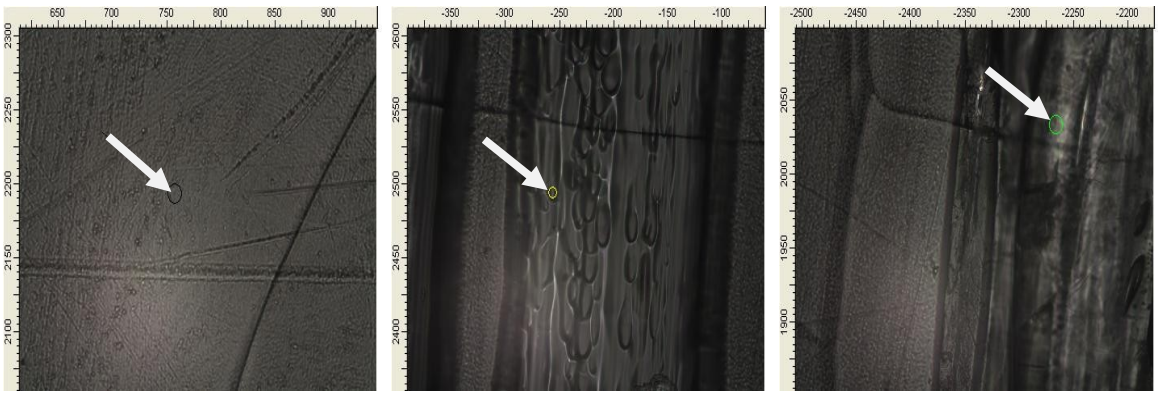

a) b) c)

Figure 4.5 Raman Microscope Images show points where Raman spectra collected a) un-irradiated area, b) melting area and c) ablation)

Figure 4.6 below shows the Raman spectra collected from different regions in the fabricated structures at (10 mW) power, P1: un-irradiated area, P2: melting area, P3: ablation area, the spectral range was from 500-1800 cm^{-1}.

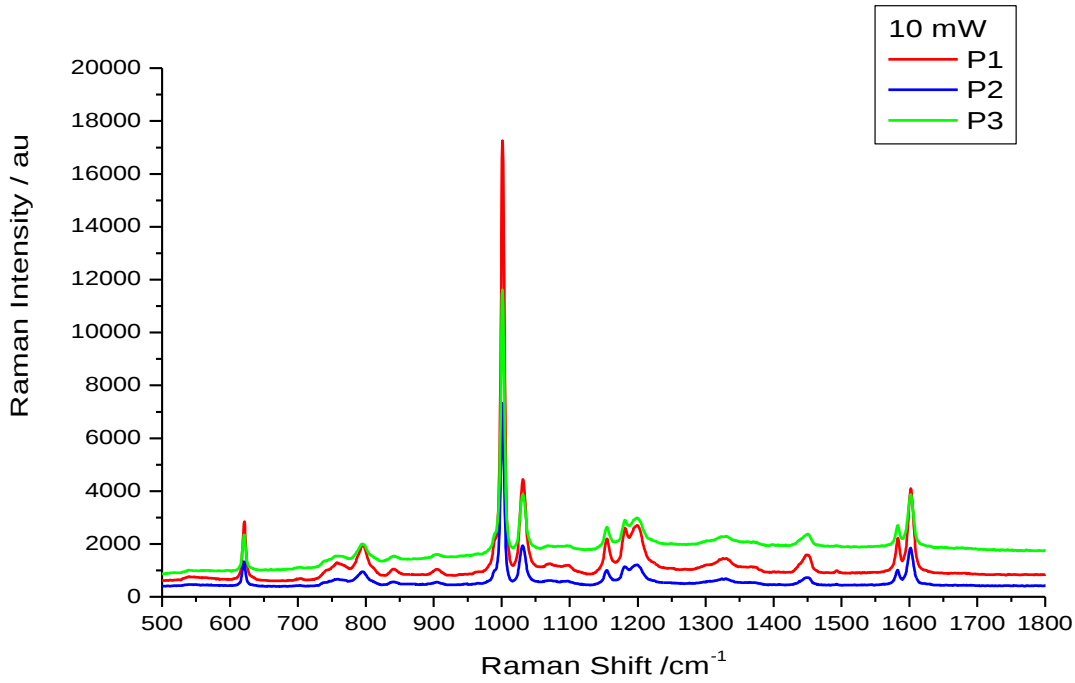

Figure 4.6 Normalized Raman spectra at un-irradiated, melting and ablation points with 10 mW

This figure shows variations in the peaks intensities and intensity of background scattering light at un-irradiated area, melting area and ablation area.

No new peak appears in the spectrum which means no formation of new bonds and so no cross-linking happened.

Absence of chain scission effects was proven by the comparison of the Raman spectra taken from the irradiated and un-irradiated part of the PMMA.

Spectra in figure 4.7 below show clearly the comparison between these spectra at un-irradiated (red line), melting (blue line) and (green line) ablation points for different separated Raman transitions, (for example band at 800 cm^{-1} belongs to main ester chain, 1000^{-1} belongs to O–CH_3 rock, 1030 cm^{-1} belongs to backbone chain C-C stretching and at 1450 cm^{-1} belongs to ester methyl group see Figure 4.4) corresponding to the irradiated area representing the absence of chain scission caused by incident radiation. The difference between the irradiated and the un-irradiated area is characterized by a decrease in the peaks intensities.

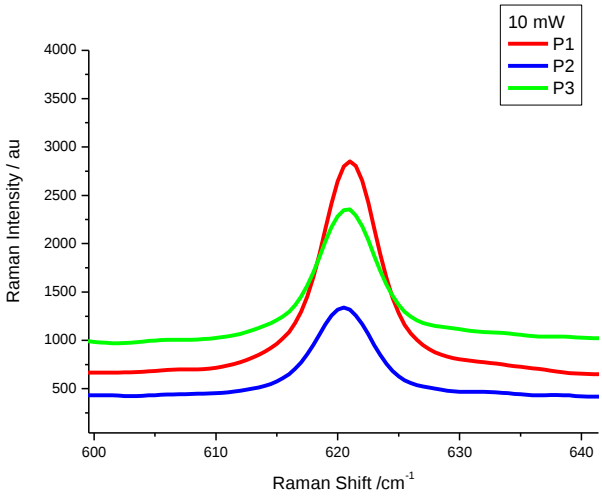

a) Raman shift 620 cm^{-1}

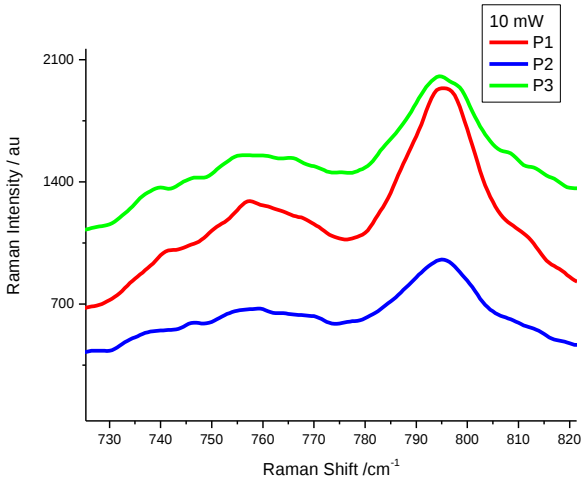

b) Raman shifts 755cm^{-1} & 800 cm^{-1}

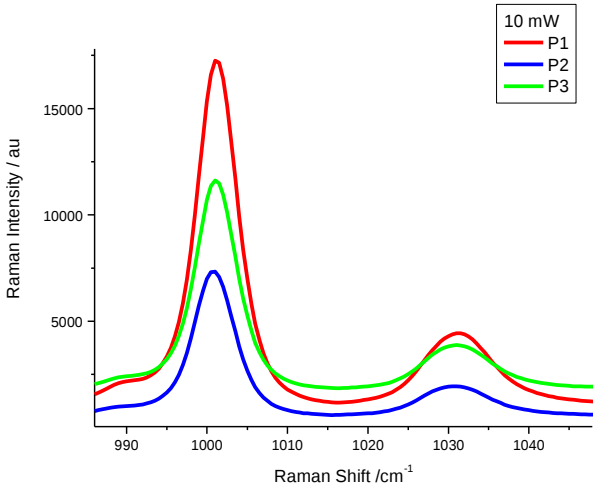

c) Raman shifts 1000 cm^{-1} & 1030 cm^{-1}

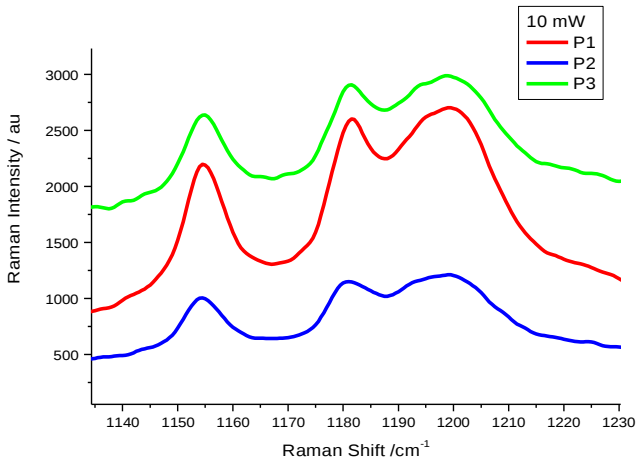

d) Raman shifts 1155 cm^{-1} & 1180-1205 cm^{-1}

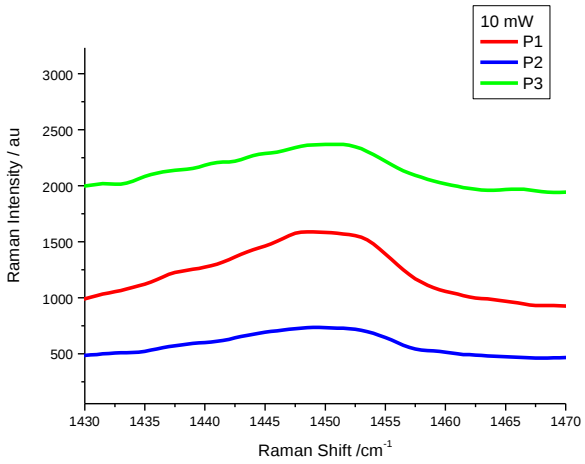

e) Raman shifts 1445 - 1460cm-1

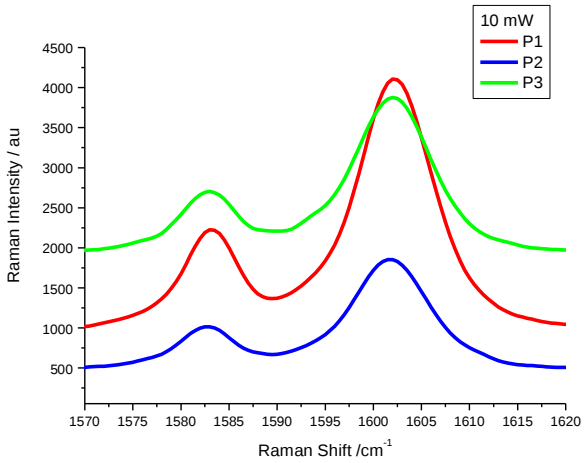

f) Raman shifts 1582 cm^{-1} & 1602 cm^{-1}

Figure 4.7 Discrete Raman spectra at un-irradiated, melting and ablation points for different transitions (a, b, c, d, e & f).

4.3 Diffraction patterns achievement

When the laser is focused into the material, the intensity is sufficiently high for multi-photon absorption to take place only at the focus. This allows refractive index modifications to be created at discrete localized sites within the bulk material, thus enabling 2-D or 3-D Bragg structures to be written into the bulk material.

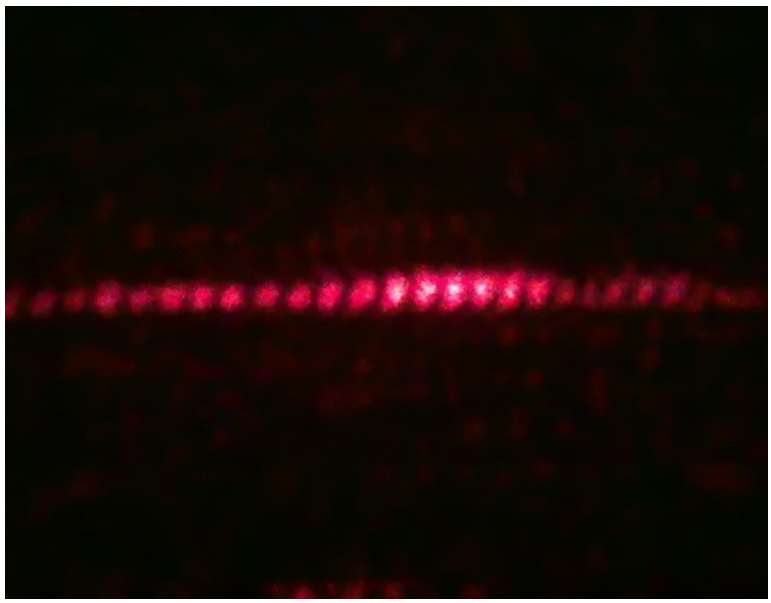

Figure 4.8 Photograph of grating diffraction pattern of the1D irradiated PMMA

Figure 4.8 show a photograph of a diffraction pattern from a grating in PMMA slab showing 22 diffraction orders. Gratings produced using these techniques diffracted the light and were easily visible to the naked eye.

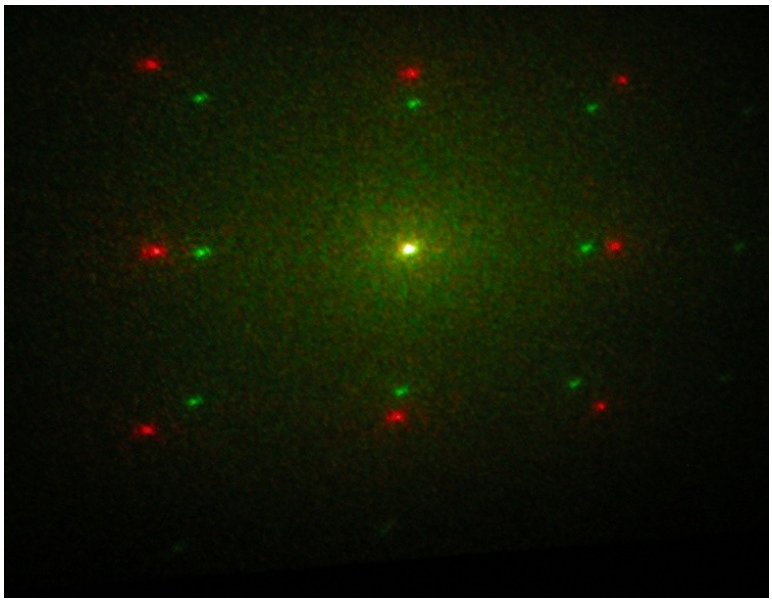

Figure 4.9 Photograph of grating diffraction pattern of the 2D irradiated Si

The induced nano-ripple surface works as Diffraction Grating. Figures (4.8 and 4.9) show the diffraction pattern by transmitting a Helium Neon laser beam through PMMA and by reflecting and diffracting from Si surface.

The change in surface scattering light intensity indicates a periodic change in optical density which may be related to the laser induced total refractive index change independent of specific molecular bond changes.

4.4 Silicon photovoltaic's Spectral Response Measurement

Scale changing of the surface reshaping occurs even at law values of the laser irradiation. Under laser pulses, the surface becomes corrugated by nanostructured hilly and valley. The spacing of these nano-channels decreases as the number of laser pulses and fluence increased. In Si photovoltaic cell the cause of formation of the nano-ripple forms is due to the optical interference of the incident and scattered laser pulses from the sample.

The texture surface reflects the incident laser pulses from back into the cell substrate (see figure 4.10), and strongly reduces the incident solar reflection and increases the absorption by generating a longer internal light path and prevent the incident light from exiting the cell.

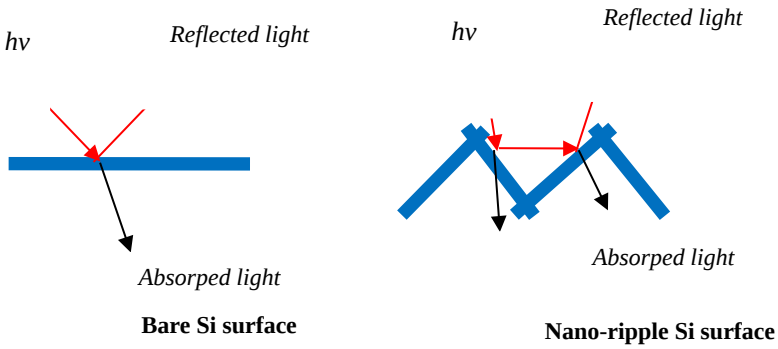

Figure 4.10 Nano-ripple effects on the light reflection and absorption

The effect of the irradiation of ultra-short laser pulses on the spectral response is shown in figure 4.11, a below. This figure shows the dependence of the responsivity versus wavelength and the role of the laser effects at room temperature. The relative response increased after the irradiation processes. From this figure one can observe that the efficiency of the irradiated sample is enhanced clearly compared to un-irradiated sample at wavelengths longer than 500nm. The responsivity of the photovoltaic cell hence is increased from 0.18A/W to 0.25A/W due to irradiation effect.

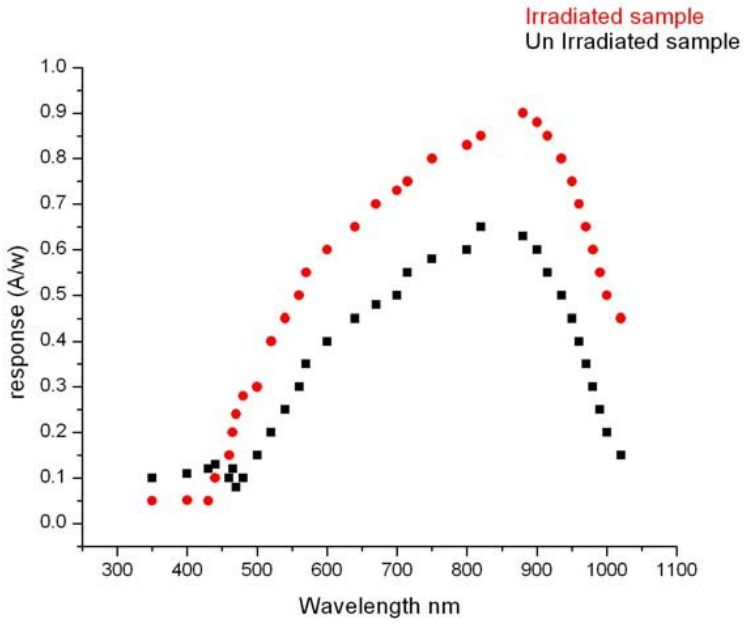

a)

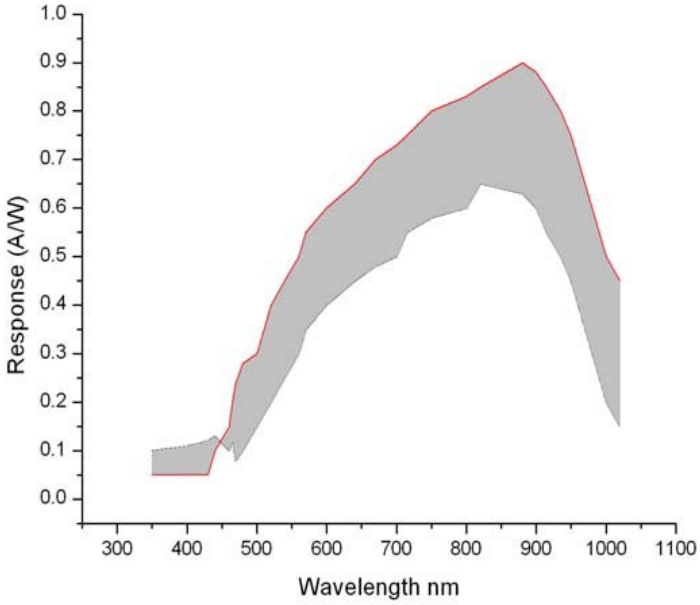

b)

Figure 4.11 Spectral responses of the irradiated and photovoltaic solar cells (a) and comparison of the spectral response curve of irradiated and un-irradiated cells (b)

The conversion efficiency of the irradiated cell was calculated using the well known equation:

$$\eta = IV/AI_o \qquad (4.1)$$

Where I is the value of the current, V is the voltage, I_o is the solar intensity and A is the solar cell area. The results show that the measured efficiency for the bare Silicon photovoltaic cell rises from 9% before irradiation to 14% after irradiation. However, the area under the response curves as shown in figures (4.11, b) indicating the total response of the irradiated samples. The

ratio of the total quantum yield before and after irradiation is increases by a factor 1.43 over the whole spectral range.

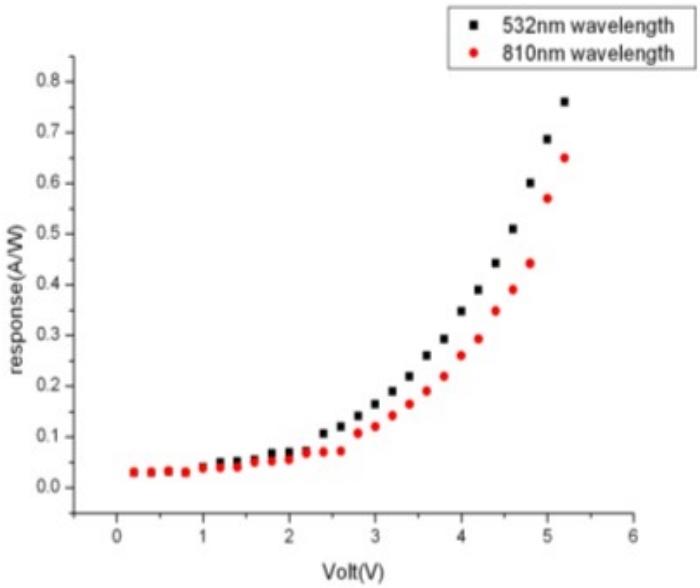

Figure 4.12 The gain response of the irradiated sample at two different wavelengths

Also the irradiation dependence on laser wavelength had been studied. The gain response curves as a function of the bias voltage for samples irradiated at different wavelengths are shown in Figure 4.12. The trend is the same at different wavelengths, 532 nm and 810 nm.

This method leads to the production of photovoltaic cells, indeed, with enhanced material responsivity and hence the conversion efficiency. Since the efficiency of the amorphous Silicon photovoltaic cells is increased from 7% to about 9% during the last 40 years utilizing different methods, the stepping to 14% efficiency must be by rearranging the micro crystal structure of the cell surface.

4.5 Conclusions

In this study, some of the versatile capabilities of laser processing to modify the surface properties of materials, in order to enhance their performance for a variety of applications, have been shown.

A textured surface was obtained in Polymethylmethacrylate (PMMA) by means of IR diode laser, 0.3 Watt at 810 nm wavelength, and in Silicon photovoltaic cell (Si) at 1kHz repetition rate, for 180fs at 387nm and 44 fs at 800nm.

SEM images, of the surface texturing in PMMA and silicon photovoltaic cell, showed laser-ablated and laser-melted and some surface topographical changes in PMMA surfaces, for silicon photovoltaic cell images show a semi periodic structure known as ripples or grooves in the sub-micrometer range

The results of Raman spectroscopic showed variations in the peaks intensities and intensity of background scattering light at un-irradiated area, melting area and ablation area. No new peak was appeared in Raman spectra which mean no formation of new bonds and so no cross-linking was happened. Absence of chain scission effects was proven by the comparison of the Raman spectra taken from the irradiated and un-irradiated part of the PMMA.

Diffraction pattern from a grating in PMMA slab showed 22 diffraction orders. The change in the light intensity indicates a periodic change in the optical density which may be related to the laser induced total refractive index change independent of specific molecular bond changes.

Gratings produced in PMMA and Silicon diffracted the light which can be easily detectable.

It is observed from the spectral response measurements, of a silicon photovoltaic cell, that the use of this method leads to improve the responsivity from 0.18A/W to 0.25A/W and the conversion efficiency of the photovoltaic cell. This technique is much cheaper and simpler than the electron beam lithography.

4.6 Applications and Future work

Further work to be presented include the investigation of temperature stability of the photo-induced gratings, UV-visible and FT infrared spectroscopic studies that illustrate the material modification mechanism, and the demonstration of grating structures written into single-mode and multimode plastic optical fibres.

Finally, the research presented here need to be extended to other classes of polymers including cross-linked elastomers, hydrogels, polyesters and polycarbonates. Developing Surface Modification from these polymers could be important in several applications.

Laser surface processing will continue to improve the performance of materials in existing applications and will open the door to new materials and novel applications that would not be possible without these unique processing capabilities.

References

[1] Bauer, M. (2010) *Raman spectroscopy of laser induced material alterations*. A Thesis Submitted in partial fulfilment of the Requirements of München University for the Degree of Doctor of Philosophy. München.

[2] Baum, A. et al. (2007) NUV and NIR Femtosecond Laser Modification of PMMA. In *the 8th International Symposium on Laser Precision Microfabrication.* Proceedings of LPM.

[3] Baum, A. (2011*) Optical characterization of PMMA phase gratings written by a 387 nm femtosecond laser*. Optics Communications 284, 2771–2774.

[4] Buividas, R. et al. (2012) *FEMTOSECOND LASER PROCESSING – A NEW ENABLING TECHNOLOGY*. Lithuanian Journal of Physics, Vol. 52,No. 4, pp. 301–311.

[5] Cheng, J. (2004) *Direct-write Laser Micromachining and Universal Surface Modification of PMMA for Device Development*. Sensors and ActuatorsB99, 186-196.

[6] Chrisey, D.B. (2000) *Appl. Surf*. Sci.154p. 593.

[7] Costas, P. G. (2009) *Transport in Laser Microfabrication*. Cambridge: Cambridge University Press.

[8] Craig, B. A. & Piqué, A., (2007) *Laser Direct-Write Processing*. MRS BULLETIN.VOLUME 32. JANUARY.

[9] Deepak, K.L.N.,,S. Venugopal, R.D. & Narayana, R. (2011) *Femtosecond laser micro fabrication in polymers towards memory devices and microfluidic applications*. Laser-Induced Damage in Optical Materials, Proc. of SPIE Vol. 8190.

[10] Ding, X., et al. (2002) *Appl. Phys*. A75(2002) p. 641.

[11] Dobrzański, L.A. & Drygała, A., (2008) *Surface texturing of multicrystalline silicon solar cells*. Journal of Achievements in Materials and Manufacturing Engineering, VOLUME 31ISSUE1November.

[12] Dongre, C. et al. (2007) Characterization of Femtosecond Laser Written Waveguides for Integrated Biochemical Sensing. *12th Annual*

Symposium IEEE/LEOS Benelux. 17-18 December 2007, Brussels, Belgium. pp. 27-30. ISBN 978-2-9600753-0-4.

[13] Fernandes, L. A. et al. (2011) *Femtosecond laser fabrication of birefringent directional couplers as polarization beam splitters in fused silica*. Optical Society of America Vol. 19, No. 13 / OPTICS EXPRESS 11992.

[14] Florea, C. & Kim A. (2003) *Fabrication and Characterization of Photonic Devices Directly Written in Glass Using Femtosecond Laser Pulses*. JOURNAL OF LIGHTWAVE TECHNOLOGY, VOL. 21, NO. 1, JANUARY.

[15] Graham, D. M., Martin, A. & Michael, J. W., (2006) *Direct laser written waveguide–Bragg gratings in bulk fused silica*. OPTICS LETTERS / Vol. 31, No. 18 / September 15.

[16] Harper, C. A. (2005) *Handbook of Plastic Processes*. John Wiley & Sons.

[17] Harris, D.C. & Bertolucci, M. D. (1978) *Symmetry and spectroscopy: an introduction to vibrational and electronic spectroscopy*. Oxford University Press.

[18] Horn, W. et al. (2012) *Electro-optical tunable waveguide Bragg gratings in lithium niobate induced by femtosecond laser writing*. Vol. 20, No. 24 / OPTICS EXPRESS 26925.

[19] Intertek (2014) *Confocal Raman Mapping*. [Online] Available from: http://www.intertek.com/analysis/raman/confocal [Accessed: 19 July 2014].

[20] Kai, C.C., Fai, L.K., and Sing, L.C. (2004) *Rapid Prototyping: Principles and Applications*. London: World Scientific.

[21] Kallepalli, L. N. D., Soma, V. R. & Desai, N. R. (2012) *Femtosecond-laser direct writing in polymers and potential applications in microfluidics and memory devices*. Optical Engineering (July 2012) 51(7), 073402

[22] Kallepalli, L. N. D., Soma, V. R. & Desai, N. R. (2012) *Spectroscopic investigation of fs laser-induced defects in polymer and crystal media*. Laser-Induced Damage in Optical Materials, Proc. of SPIE Vol. 8530.

[23] Kallepalli, L. N. D. & Desai, N. R., (2013) *Comparative Study of Defect Formation in Femtosecond Laser Irradiated Polymers and Crystalline Media*. Photonics and Optoelectronics (P&O) April (2013) Volume 2 Issue 2.

[24] Kazuyoshi, I., (2006) *Laser microengineering of photonic devices in glass*. JLMN-Journal of Laser Micro/Nanoengineering, Vol. 1, No. 1,

[25] Kopitkovas, G. et al. (2003) *Microelectron*. Eng.67p. 438.

[26] Kovačević, A. et al. (2007) *Laser–PMMA Interaction and Mechanical Stresses*. ACTA PHYSICA POLONICA A No. 5, Vol. 112.

[27] Krishnan, R. et al. (2006) *Laser Surface Modification of Thermal Sprayed Aluminium Oxide Coating*. Surface and Coatings Technology, 200 – 279.

[28] Kro, D. M. et al. (2004) Fs-Laser Fabrication of Photonic Structures in Glass: the Role of Glass Composition. *Fifth International Symposium on Laser Precision Microfabrication*, Edited by I. Miyamoto, H. Helvajian, K. Itoh, K. F. Kobayashi, A. Ostendorf, K. Sugioka, Proc. of SPIE Vol. 5662 (SPIE, Bellingham, WA.

[29] Lenzner, M. (1999) *Appl. Phys*. A68p. 369.

[30] Luppnow, G. R. et al. (2003) *Raman Spectroscopy*. J. Raman. Spec. 34, 743.

[31] Marouf, A. A. S. et al. (2014) *The Role of Photonic Processed Si Surface in Architecture Engineering*. Volume 3. USA: Study of Civil Engineering and Architecture (SCEA).

[32] Michael, J. Hollas (2004) *MODERN SPECTROSCOPY*. Fourth Edition, London: John Wiley & Sons Ltd.

[33] Oliveira, V. et al. (2012) *Laser surface patterning using a Michelson interferometer and femtosecond laser radiation*. Optics & Laser Technology 44, 2072–2075.

[34] Piacton (2014) *Raman Spectroscopy Basics*. [Online] Available from: www.piacton.com [Accessed: 11 July 2014].

[35] Pique, A. (2003) *Surf. Coat. Technol*. 163p. 293.

[36] Piqué, A. & Chrisey, D.B. (eds) (2002) *Direct-Write Technologies for Rapid Prototyping Applications*. San Diego: Academic Press.

[37] Pronko, P.P. et al. (1995) *Opt. Commun*.114 p. 106.

[38] Singh, M. K. et al. *Integrated Biomimemic Carbon Nanotube Composites for Biomedical Applications*. Available from: http://www.intechopen.com/books/biomedical-engineering-technical-applications-in-medicine/integrated-biomimemic -carbon-nanotube-composites-for-biomedical-applications. [Accessed: 20th May 2014].

[39] Taleb, A. M. et al. (2011) *Nanostructure Formation in Silicon Photovoltaic Cells by Femtosecond Laser Pulses* . Materials Science Forum Vol. 670 pp 118-12.

[40] Tan, B., Narayanswamy, R. S. & Venkatakrishnan, K., (2005) *Direct grating writing using femtosecond laser interference fringes formed at the focal point*. J. Opt. A: Pure Appl. Opt.7169–174.

[41] Taranu, A. et al. (2010) *RAMAN MAPPING OF FEMTOSECOND LASER WRITTEN PHOTONIC STRUCTURES IN POLYMETHYLMETHACRYLATE*. © ICPOF.

[42] Teixidor, D. & Ciurana, J. (2012) *Nanosecond Pulsed Laser Micro-Machining of PMMA-based Microfluidic Channels*. Proceedings of NAMRI/SME, Vol. 40.

[43] Vishnubhatla, K.C. et al. (2008) *Inscription and characterization ofmicro-structures in silicate, FOTURAN™ and tellurite glasses by femtosecond laser direct writing*. Commercial and Biomedical Applications of Ultrafast Lasers VIII, Proc. of SPIE Vol. 6881.

[44] Wikipedia (2014) *Functionalization of Antimicrobial Surfaces* [Online] Available from: “http://en.wikipedia.org/wiki/Functionalization_of_Antimicrobial_ Surfaces [Accessed: 21 Augustus 2014].

[45] Wikipedia (2014) *Silicon*. [Online] Available from: http://en.wikipedia.org/w/index.php?title=Silicon&oldid=620615893 [Accessed: 21 Augustus 2014].

[46] Zoubir, A. et al. (2002) Technology developments towards the practical use of femtosecond laser micro-materials processing. *High-Power*

Laser Ablation IV. Claude R. Phipps, Editor, Proceedings of SPIE Vol. 4760.

[47] Zoubir, A. et al. (2003) *Practical uses of femtosecond laser micro-materials processing*. Appl. Phys. A 77, 311–315.

[48] Zoubir, A. et al. (2004) *Femtosecond laser fabrication of tubular waveguides in poly(methyl methacrylate)*. OPTICS LETTERS / Vol. 29, No. 16 / August 15.